The effect of synthesis method and Al-doping on structure and thermoelectric properties of ZnO

Nikita Kaur Thind

Master Thesis
Materials, Energy and Nanotechnology

Department of Physics
Faculty of Mathematics and Natural Science

University of Oslo

Spring 2018

Acknowledgements

This thesis is submitted as part of the master's degree in Material Science and Nanotechnology, with the department of physics at the University of Oslo. The project has been performed in the research group Structure Physics and Solid State Electrochemistry from August 2016 to May 2018.

First of all I would like to thank and express my gratitude to my supervisors Anette Gunnæs, Truls Norby and Matthias Schrade for their motivation and encouragement throughout the this project and especially at the very end. Furthermore, I would like give a special thanks to Monika Løberg for always supporting and motivating me, and having the time for countless of discussions. Further I would like to thank Phoung D. Nguyen for help with STEM results and Matylda Guzik for XRD refinement, teaching and advice. Big thanks is owed to Temesgen Debelo, Ole Bjørn Karlsen and Xin Song for all their teaching, help with measurements and results. I am very grateful to all members associated with the both research groups for showing interest in my thesis and providing the best possible scientifically and socially environment.

Special thanks is attributed to Jenny and Kristin for always being there for me and pushing me forward. Furthermore, I would like to thank my family, my brother Sagar for all his love and support. My parents, for always believing in me and convincing me that anything is possible as long as I put my heart into it. Last, but not least I would like to thank to Tarnjit for always being there, having faith in me and encouraging me.

Abstract

Thermoelectric (TE) generators can convert waste heat into electrical energy. However, current high end TE materials are either too costly, not environmentally friendly or have too low efficiency to make a big impact on the energy market.

High figure-of-merit TE materials are in general known to show high electrical conductivities and Seebeck coefficients, and low thermal conductivities. Al-doped ZnO is found to be a promising TE n-type semiconductor for high temperature applications.

In order to learn more about the Al-doped ZnO material system, the effect of synthesis methods on structure and TE performance has been investigates. An extensive study including three synthesis routs (one sol-gel and two solid-state with ball milling) have been performed on three different Al-ZnO compositions (0, 1 and 5 mol % Al). The samples have been extensively characterized by combining X-ray diffraction (XRD) and analytical electron microscopies (SEM, TEM and STEM combined with EDS) with electrical and thermal analysis.

It was found that $ZnAl_2O_4$ particles exist in all samples with added Al, although not detectable with XRD for the 1 mol% Al compositions. The synthesis methods and Al composition have an impact on the size of the $ZnAl_2O_4$ particles and the ZnO grains. The sol-gel process resulted with the smallest $ZnAl_2O_4$ particles followed by planetary and roll milled samples. However, this variation in microstructure was not found to have any impact on the thermal conductivity.

The charge carrier concentration and resulting electrical conductivities were found to differ. Based on the measured Seebeck coefficients, the sol-gel samples showed no increase in carrier concentration upon Al additions and the electrical conductivities were found to be even lower than intrinsic ZnO. Both ball milled processes applied resulted in similar and Al content dependent carrier concentrations consistent with Al doped ZnO. The electrical conductivity of the ball milled samples were, however, found to be Al content dependent. In general, the electrical conductivities were found to be higher for the samples with 1 mol% Al content although the carrier concentration was found to be higher in the 5 mol% samples. In particular, the sample prepared by the low energy roll ball milling showed remarkably higher electrical conductivities (~250 S/cm at T~200 ^{o}C) compared to the other ball milled samples (~50 S/cm). The roll milled samples showed an increase in electrical conductivity upon cycling, contrary to the planetary milled. The trend was reproducible, but the trend has not been reported and the reason is unknown. A structural difference between the sample with high electrical conductivity

and the others was presence of a thin layer of the secondary phase decorating the ZnO grain boundaries, which is not to us previous reported finding.

A figure of merit of 0.13 was obtained at 800°C for roll ball milled 1 mol% Al sample. This is consistent with reported values of similar compositions in the literature.

Contents

Chapter 1

Introduction

Because of increasing population and higher living standards, the energy consumption is increasing. Most of today’s energy comes from fossil fuels and the impact these resources have on the environment has further increased the political and social unrest in parts of the world. Fossil fuels are a limited resource and due to its effects on the environment, the need for more renewable energy and better energy management is needed in order to produce sufficient amounts of energy and reduce the emission of greenhouse gasses. There is currently a lot of research on environmentally friendly energy harvesting based on solar energy. However, we also have an energy source in waste-heat that is getting more attention.

With a thermoelectric generator (TEG) waste-heat can be converted into electrical energy without any moving parts or harmful emission and might play an important role in the energy management in the future. As in the case of other energy transforming processes, there is a need to increase the conversion efficiency of the energy transforming process to make better use of the waste-heat. At the same time, abundant and non toxic elements should be used in order to make TEGs economical sound and feasible to implemented on a larger scale with impact on energy management.

1.1 Thermoelectric generators

A thermoelectric generator is a solid state devices with pared thermoelectric n-type and p-type legs classically connected through metallic electrical pads as illustrated to the right in Figure 1.1. A thermoelectric module, as illustrated to the left, consist of an array of these couples arranged electrically in series and thermally in parallel. When a temperature gradient is imposed across the device, it results in a voltage that can be used to drive a current through a load or device. Alternatively, if an electrical current goes through such a device a heat gradient will be created and the device is generally referred to as a Peltier element.

The maximum conversion efficiency for a thermoelectric generator is calculated according to the equation [1]

$$\eta = \frac{\Delta T}{T_{hot}} \frac{\sqrt{1 + ZT_{aver}} - 1}{\sqrt{1 + ZT_{aver}} + T_{cold}/T_{hot}} \tag{1}$$

where T_{hot} and T_{cold} are the temperatures at the hot and cold side, ΔT is their temperature difference and T_{aver} is the temperature average. $\Delta T/T_{hot}$ represents the Carnot efficiency and ZT is the figure of merit of the p-n couple.

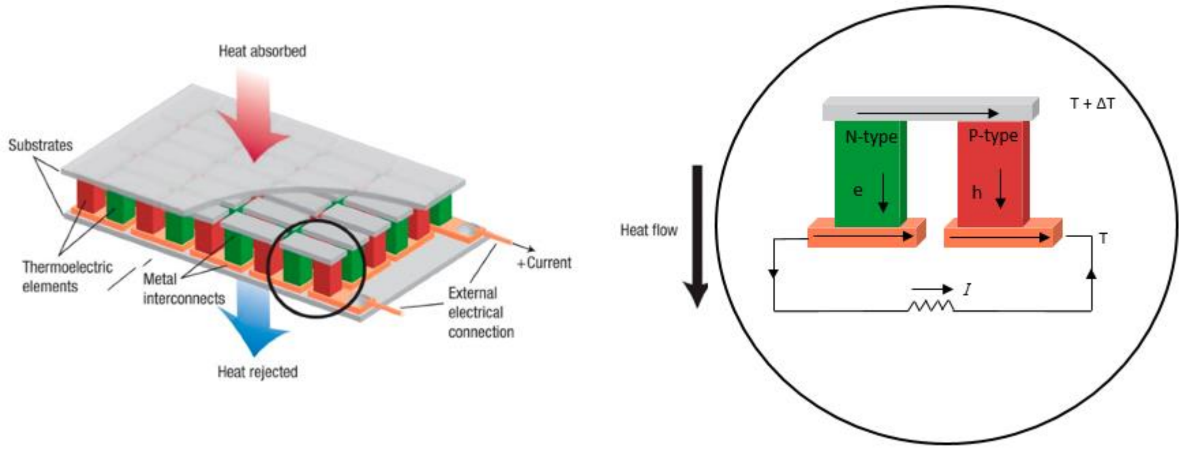

Figure 1.1: An illustration of a thermoelectric generator (left) and a thermoelectric module (right), modified from [2].

1.2 Figure of merit

The figure of merit of the p-n couple is denoted ZT, while the potential of a material for thermoelectric applications is described by zT and determined by

$$zT = \frac{\alpha^2 \sigma T}{\kappa} \tag{2}$$

where α is the Seebeck coefficient, σ is electric conductivity and κ the thermal conductivity. Higher zT indicates a more effective material, with zT≈1 as an upper limit for the last 30 years. Tuning of one of these material properties will affect the others as illustrated in Figure 1.2 where an increase in carrier concentration is correlated with an increase in electrical and thermal conductivities and a drop in the Seebeck coefficient. The Seebeck coefficient and electrical conductivity make up the power factor $\alpha^2\sigma$, hence it is also correlated with the carrier concentration, as seen in Figure 1.2, must be optimized to achieve good TE performance.

Beside optimizing the power factor, another strategy is to to increase zT is to reduce the thermal conductivity. The total thermal conductivity (κ) consisting of an electronic (κ_e) and a lattice contribution (κ_L)

$$\kappa = \kappa_L + \kappa_e \tag{3}$$

Since the power factor is correlated with κ_e, an increased zT can be achieved if the thermal lattice conductivity is reduced.

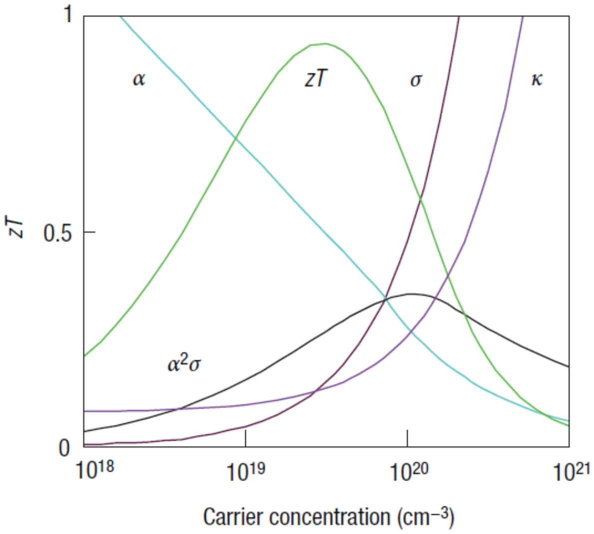

Figure 1.2: Figure of merit, zT, as a function of carrier concentration [2].

1.3 Thermoelectric materials and strategies of improvement

Over the past decade the interest in the field of thermoelectrics has increased and various materials have been reported. Different materials for different operation temperature has been reported as illustrated in Figure 1.3, whereas over the past 40 years various Bi_2Te_3, $Si_{1-y}Ge_y$ and PbTe systems have been studied and optimized [3]. Due to poor durability at higher temperatures, high cost and high toxicity they are incapable of wide commercialization.

Oxides have in the past received little attention since they generally show high thermal and low electrical conductivity. However, when it was reported that $NaCo_2O_4$ showed a high *zT* of 0.7-0.8 at 1000K the interest for TE oxides increased [4]. Oxides are in general favourable for high-temperature application as illustrated in Figure 1.3 due to their high temperature stability, non-toxic elements and the possibility for low-cost material synthesis.

The optimal TE material should have a phonon-glass and electron-crystal properties, which means low thermal conductivity such as for glass, while obtaining a crystalline electrical conductivity. As earlier mentioned, there are two general strategies for enhancing zT, focusing on either optimizing the power factor or minimizing the thermal conductivity.

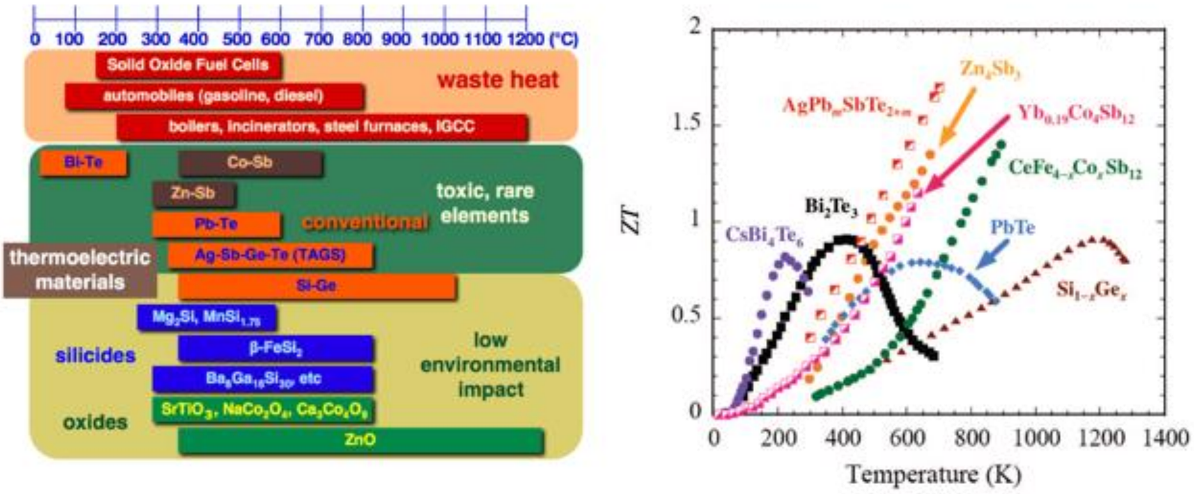

Figure 1.3: Waste heat and operation temperature for various thermoelectric materials (left) [3] and figure of merit, zT, for various thermometric materials (right) [5].

For the latter there are three approaches. The first is to scatter phonons within the unit cell by point defects or rattling atoms. This has been demonstrated for skutterrudites and clathrates where structural voids have been filled which “rattler” atoms that have the ability to scatter phonons and reduce the lattice themal conduction [2]. The second approach is to create a complex crystal structure, like layered structures, causing a decrease in the thermal conductivity without affecting the electron transport [2]. The third approach is to increase phonon scattering by nanostructuring [2, 6]. The nanostructures, like fine precipitates, should be evenly distributed in the matrix to increase the phonon scattering events and hence reducing the lattice contribution to the thermal conductivity. A minimum lattice thermal conductivity can be acchived when phonons have a mean free path equal to the interatomic spacing.

1.4 Al-doped ZnO based thermoelectric

Zinc oxide is an n-type semiconductor known for its wide bandgap of about 3.3 eV [7]. Research on ZnO has been going on for many decades due to its potential within many fields such as electronics, photonics, acoustics, and sensing devices [7]. ZnO have attracted a lot of attention due several factors including the easiness of adjusting the electrical conductivity by adding impurities such as Al, Sb, Mn [8]. Despite a vade application range and research done, the thermoelectric properties were not discovered until Ohtaki *et al.* doped it with Al and the *zT* was significantly increased [9].

In the wurtzite type structure of ZnO there is strong covalent bonding. The simple crystal structure and light element composition makes ZnO suffer from high thermal conductivity ranging from 49 $Wm^{-1}K^{-1}$ at 300K to 10 $Wm^{-1}K^{-1}$ at 1000K [10]. Al-doping introduce excess charge carriers, increasing the electrical conductivity from 2.5 Scm^{-1} in pure ZnO to 700 Scm^{-1} at room temperature for 5 mol% Al [11]. Despite a high thermal conductivity of 40$Wm^{-1}K^{-1}$ for a 2 mol% Al-doped ZnO sample, a zT of ~0.3 at 1000°C was achieved by Tsubuta *et al.* [10] and is among the highest reported values for n-type oxides [3].

Nanostructuring has been shown to be more effective than incorporating dopants in order to increase zT [12, 13]. zT of 0.44 at 1000K by a microwave-aided hydrothermal method is reported [12]. They were able to lower the thermal conductivity to 2.8 $Wm^{-1}K^{-1}$ at room temperature and is as shown in Figure 1.4 is currently the highest zT reported for purely Al doped ZnO come upon in the current study.

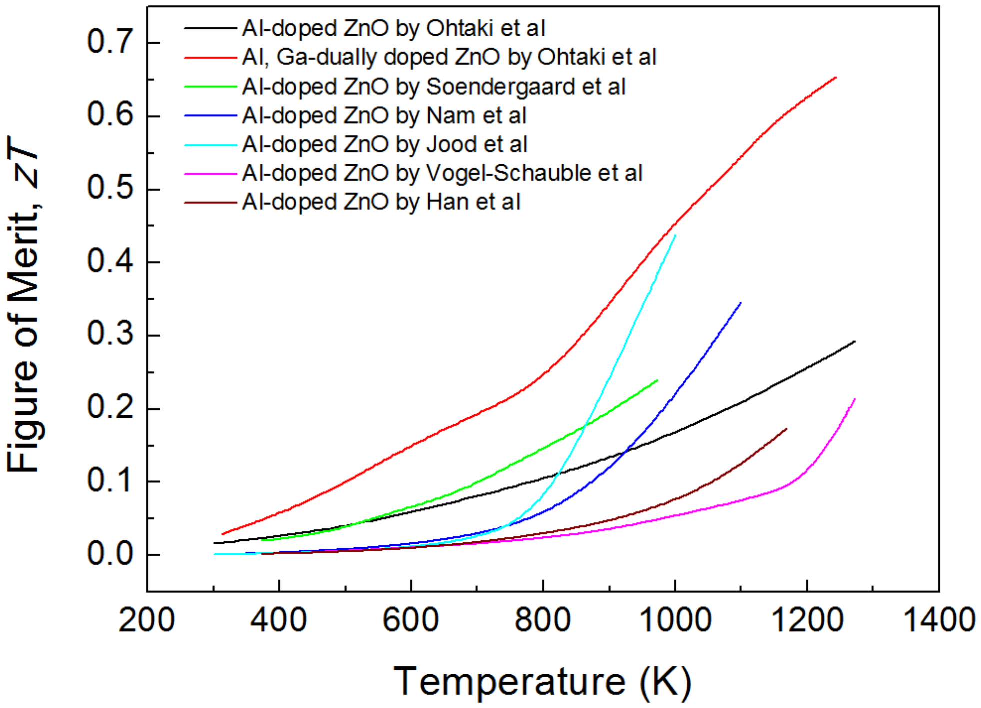

Figure 1.4: Reported figure of merit values as a function of temperature for Al-doped ZnO [14].

A low thermal conductivity has also been reported for a sol-gel synthesis method with nitrates resulting in a zT of 0.34 at 1073K [13]. They reported that the nanostructuring mainly affected the electrical and thermal conductivity, rather than the Seebeck coefficient.

1.5 Project aim

In the current project, the main scientific goals were to:

-Investigate the effect of the selected synthesis routs on the structure and TE properties of Al-doped ZnO. Three different synthesis routs were used including one sol-gel method and two solid state processes employing high and low energy ball milling to produce powders that were subsequent sintered. A variety on structure and properties could be anticipated.

-Investigate the effect of Al-doping on the structure and TE properties of Al-doped ZnO. For the different synthesis routs Al-compositions of 0, 1 and 5 mol% was prepared for a comparative study. The 0 mol% compositions are prepared as reference samples and the 1 and 5 mol% fall into the category of compositions where high zT has been reported in the literature. With the lower Al composition, one aimed to be close to the solid solubility range of Al in ZnO at high temperatures. The 5 mol% Al composition represents a composition well beyond the solubility range of ZnO where precipitates or secondary particles could be anticipated. If the size of the precipitates or particles are in the nanorange, one could anticipate high zT values.

- There was a specific goal to combine several characterisation techniques on the same samples to get a more complete picture of correlating factors and being able to calculate the zT of the best sample. A combination of electron microscopy, X-ray diffraction and thermal and electrical characterisation was performed.

Chapter 2

Theory

2.1 Synthesis

In this section a brief introduction to the synthesis methods applied in this thesis will be given based on the theory presented in [15-17].

2.1.1 Solid state synthesis

The most common method in solid-state synthesis is the ceramic method. Two or more compounds are mixed together, pressed into a pellet and calcinated to form the product. Simple starting materials like compound oxides and no waste products make the ceramic method a desirable synthesis approach. A drawback might be poor mixing at the atomic scale which might lead to an inhomogeneous product.

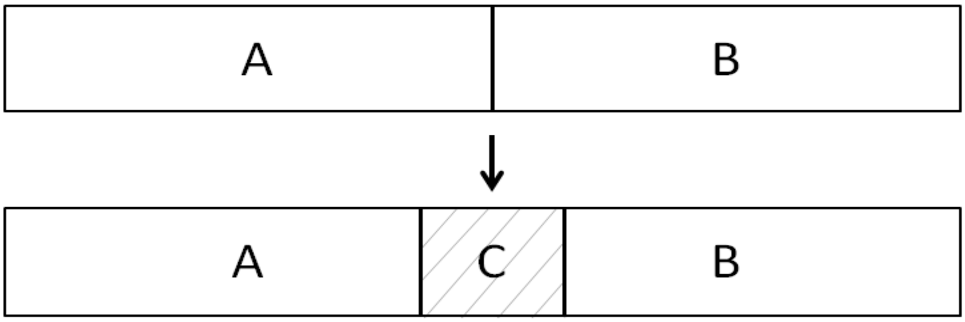

Figure 2.1: Illustration of a product C forming between reactants A and B, adapted from [15].

Contact between reactant A and B is important for the formation of product C. When product C is formed, it forms a contact barrier that increases the distance between reactant A and B. This results in increasingly longer diffusion paths and slower reaction rates. The formation of product C is illustrated in Figure 2.1. Development of the product layer C in one dimension is given by

$$\frac{dx}{dt} = k * x^{-1} \tag{4}$$

where x is the amount that has reacted (thickness of product C), t is time and k the rate constant. To overcome the problem that arises due to increasing distance between A and B, two approached might be applied: the calcined pellet can be crushed and the heat treatment repeated or the sintering temperature can be increased.

Mechanical milling

An important factor to promote a homogenous product is decreasing diffusion lengths. A common way to reduce these lengths is by decreasing the particle size of the reactants. Creating new surface is an energy consuming process. Energy can be transferred to the powder by mechanical milling, which, in addition to breaking particle, might also change the particle shape. The mechanical energy will increase defect density and generate clean surfaces. The contact area between particles increases with decreasing particle size. This reduces the diffusion length of ions which enhances the reaction rate at lower temperature.

The transfer of energy to powder can be done by either indirect or direct milling where the difference is how the energy is transferred to the powder. In direct milling, the kinetic energy is transferred directly from a shaft or roller to the particles. Some common used direct mills are attritor mill and pan mill. For indirect milling, the kinetic energy is transferred to the milling body and then to the milling medium before it interacts with the powder. It should also be kept in mind that gravitational and centrifugal forces further influence the milling medium. Some common types of indirect milling are tumbler ball milling, vibratory mill, planetary ball mill and roll ball mill. Planetary ball and roll ball mill are illustrated in Figure 2.2 and will be introduced in more detail below.

In addition to the type milling, other parameters such as the hardness and particle size of the powder, size and number of balls used, milling time, rotation frequency, temperature, and wet or dry milling conditions might influence the resulting powder. Some of these parameters will be discussed in the following.

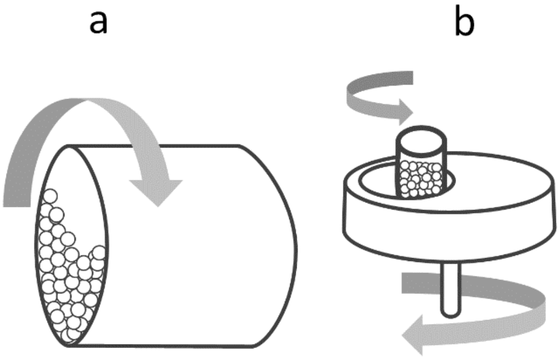

Figure 2.2: Illustration of (a) roll ball milling and (b) planetary ball milling.

Type of mill: A ball mill rotates around a horizontal axis as shown in Figure 2.2a. Increasing the diameter of the milling body increases the operation efficiency. This because, when increasing the height of the grinding media, the distance the media will fall down is also increased, and thus the impact energy of the grinding media will be greater. This is often referred to a gentle milling technique since a lower rotation frequency is used.

Planetary ball milling is illustrated in Figure 2.2b, where the jar is mounted on a sun wheel rotating around a vertical axis in the opposite direction of the jar. In this milling technique, a larger milling body will increase the kinetic energy because of larger traveling distances for the grinding medium give higher kinetic energy. This milling technique can operate at a higher rotation speed compared to the ball milling presented above, and is often referred to as a more energetic process.

Grinding medium: The mass of the grinding medium effects the velocity, hence the kinetic energy. Dense packing of the grinding medium reduces the mean free path, while dilute distribution minimizes the collision frequency. In addition to the amount of balls, the ratio of balls-to-powder should be taken into account so ensure enough space for the balls and powder to move around freely. To enhance the milling efficiency different shapes and sizes of the grinding medium can be used such as spheres, cylinders, cubes, cylpebs etc. Also a mix of small and large balls will give higher collision energies.

Powder: The resulting morphology of the milled powder depends on whether the material is ductile or brittle. Brittle materials are continuously fractured when exposed to high-level impact forces. For ductile materials, interlocking of spongy or rough surfaces, molecular interactions by van der Waals forces or agglomeration can occur. In ductile-brittle systems, the brittle particles will be reduced in size, while the ductile particles acquire elongated shapes.

2.1.2 Wet Chemical synthesis: Sol-gel

Sol-gel synthesis is a wet chemical synthesis method used to obtain a homogenous mixture at the atomic level. It is used for inorganic solids and enables control over particle size and morphology. Several sol-gel methods exist, but only the citrate method will be introduced here.

The citrate method can be divided into several key steps: precursor preparation, sol-formation, the formation of gel and the calcination. Each step will be described below.

Precursors

Many transition metal- and rare earth oxides have poor solubility in water and are therefore not suitable for the citrate method. On the other hand, salts such as nitrates or acetates are soluble in water, thus providing a way to get metal ions in solution.

Sol-formation

Sol is an abbreviation for colloidal solid particles. To form the sol, ethylene glycol is added to the mixture at this step, in addition to citric acid as a complexing agent, while the solution is heated to a moderate temperature (~80°C) to form a viscous liquid. During mixing, the nitrate salt solution and ethylene glycol citric acid can fully protolized and be present as citrate, illustrated in Figure 2.3. The citrate binds to cations in the solution, which forms a complex where the cation is bonded to the oxygen ions the citrate which binds the cations. At his step a homogenous precursor containing metal-citrate chelate complexes is obtained. This is illustrated as the first step in Figure 2.4.

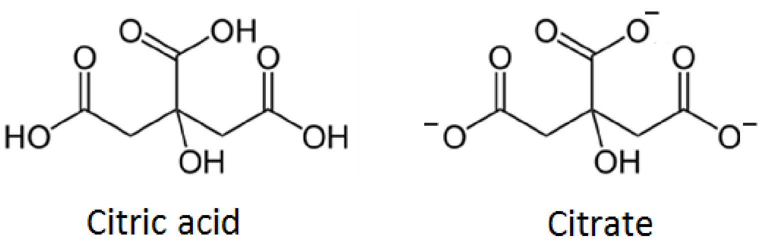

Figure 2.3: Structural formula of citric acid (left) and protolized to citrate (right).

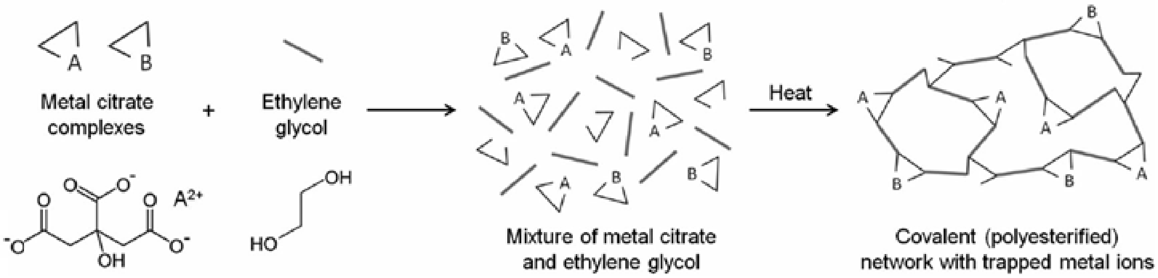

Figure 2.4: Illustration of making metal/organic gels, modified from [16].

The same precursors can give different structures with small changes in experimental parameters such as temperature, heating rate, time, ethylene glycol to citric acid ratio and pH. The homogeneity and stability of the solution and binding of citrate to metal ions, depend strongly on the pH. Low pH causes protonation of the citrate and high pH precipitation of metal hydroxide. pH control is therefore important for homogeneity and final particle size.

Formation of gel

The gel is a 3-dimesional network that extends through the fluid as shown in the last step of Figure 2.4. Water evaporates when the solution is heated to ~100°C, and the solution then forms an extended covalent network with the cation locked certain positions. A sponge-like product is formed due to large volumes of gases evolving.

Calcination

After the gel is dried, it is crushed and sintered. A combustion for organic compounds will take place at 400-700°C. During this heat treatment, the organic framework will decompose and form a xerogel. The sample is now an airy amorphous powder.

2.1.3 Sintering

When the system is heated it will try to decrease its surface free energy by decreasing its total surface area. This is reached by mass transport that joins the powder particles together. The sintering process can be distinguished through three stages (Figure 2.5):

Initial stage: At this stage particles start to grow together and form necks in the contact area, referred to as neck-growth. The particles fuse together and the contact area increases. Surface diffusion is often the dominant mass-transport mechanism during early stages of neck growth.

Mass is only transported from convex to concave areas. Only a few percentage of shrinking occurs at this stage.

Intermediate stage: The neck growth continue to decrease the distance between particle centres thus increasing the grain boundaries. Pores start to be discontinuous, and usually only closed pores remain at grain boundaries. At this stage the bulk transport mechanisms, grain boundary and volume diffusion, occurs causing material to migrate from the inside to the surface. This results in contact flattening and densification. At this stage volume of the component decrease due to densification (5-20%).

Final stage: This step happens much slower than the two previous stages. At this point, most pores are closed and will shrink. Complete removal of pores can occur, giving a fully dense material. Alternatively, large grains grow at the expense of small ones and the closed pores are isolated at triple points or inside the grain matrix.

To achieve considerable sintering, the material must be heated to 2/3 of the melting temperature [15, 18]. Beside the temperature and sintering time, other parameters such as particle size, particle packing and particle shape affect the sintering process. Material transport occurs faster over shorter distances, and less material needs to be transported to fill small pores. Furthermore, small particles will have high surface energy and therefore lower the sintering temperature. Beside this, denser particle packing increases the number of contact points and hence the relative density. This allows densification to occur faster and with less volume shrinkage. Particles that pack poorly sinter poorly. Particles with irregular shape will sinter faster, due to high surface area to volume, compared to equiaxed particles.

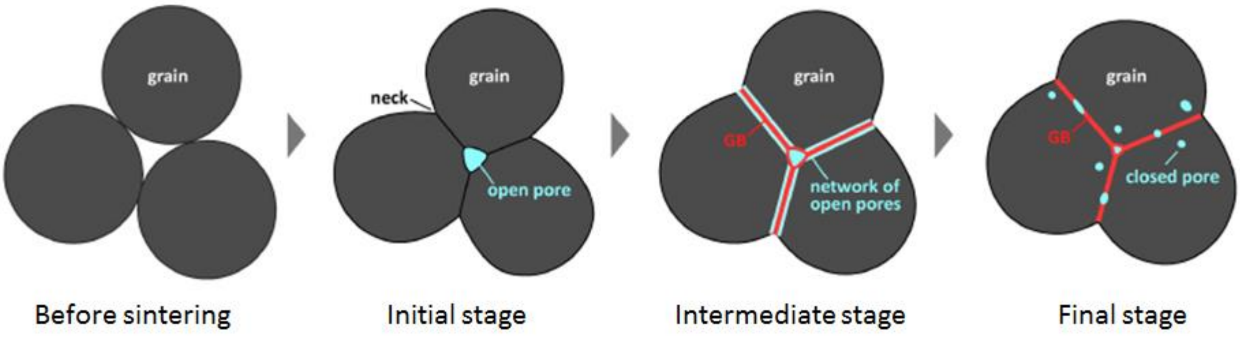

Figure 2.5: Illustration of different stages of sintering modified from [19].

2.2 Electron microscopy

This section will give a brief introduction to the field of electron microscopy and some main types of instruments and techniques, based on [20, 21]

he two electron microscopes utilized in this project are scanning electron microscope (SEM) and transmission electron microscopes (TEM), illustrated in Figure 2.6. Common for both types of microscopes is that electrons are generated in an electron gun and passed through a lens system made up of electromagnetic lenses. In the gun, electrons are emitted from an electron filament, accelerated and focused. The path of the electrons along the column are controlled by electromagnetic fields (lenses and deflectors), as illustrated in Figure 2.6. The magnetic field strength, and thus the path of the electrons through the column, can be varied by changing the electric current in the coils producing the field.

The main differences between the instruments are related to the thickness of the specimens investigated and the acceleration voltage commonly used. In a SEM, the acceleration voltage is in general low (~30 kV) and the sample can be several cm thick. The electrons which are detected are backscattered or secondary electrons, escaping from the sample surface. In a TEM the electrons are in general accelerated to much higher voltages (~60-300 kV) and the sample must be thin, less than 100nm . The electrons detected are those transmitted through the sample.

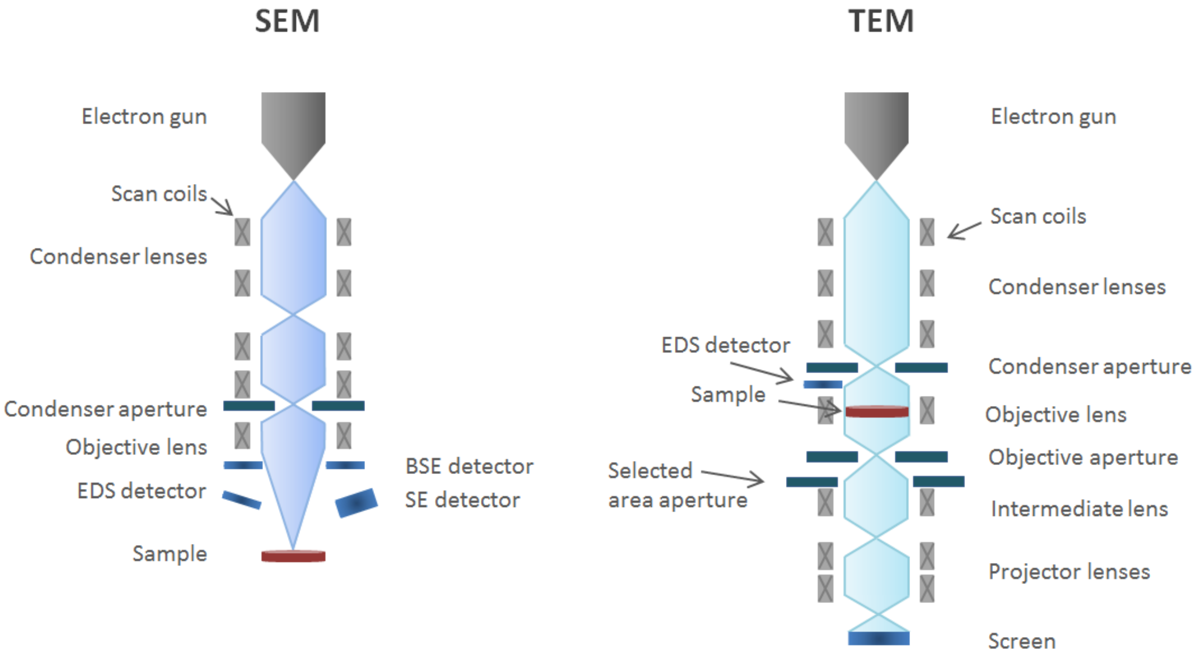

Figure 2.6: Illustration of instrumentation of SEM (left) and TEM (right).

An image of the topography of a sample can in general be obtained by SEM as well as images from flat surfaces showing an overview of the microstructure, larger particle morphologies and compositions. Small precipitates and defects such as dislocations and grain boundaries can be analysed by (S)TEM as higher resolution is needed to resolve them. Diffraction data from the TEM can in addition be used to give crystallographic information.

2.2.1 Energy Dispersive Spectroscopy

X-rays are emitted when the electron beam interacts with the sample. These are gathered by a detector above the specimen for quantitative analysis. This is used in SEM, TEM and STEM. As illustrated in Figure 2.7, an incident electron excites an electron in the inner shell leaving a vacancy. The vacancy is filled by an electron from the outer shell falling in the inner shell; emitting a characteristic X-ray. The illustration in Figure 2.7 shows that the characteristic X-rays is emitted from the volume beneath the surface. The spectrum might not correspond to what is observed from the contrast in a backscattered electron (BSE) image as the X-rays comes from a larger volume than the BSEs. The specimen should be flat, because a rough surface may interfere with the take-off angle for the emitted X-ray.

Both microscopes can have a detector for X-ray energy dispersive spectroscopy (EDS) located above the sample as shown in Figure 2.6 for compositional analysis. The volume from where the X-rays are generated will depend on the acceleration voltage, thickness and composition of the specimen analysed (see Figure 2.8 for interaction volume in a thick specimen) and hence corresponding EDS maps from TEM and SEM will differ with respect to resolution.

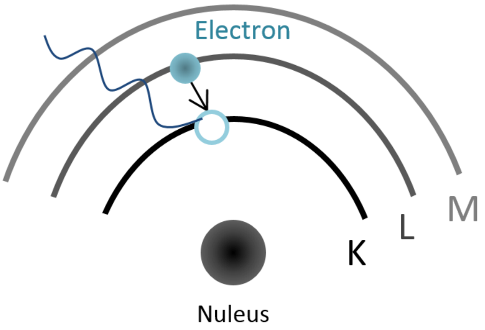

Figure 2.7: Emission of a characteristic X-ray.

2.2.2 Scanning Electron Microscopy

High-energy electrons interacting with the specimen can scatter either elastically or inelastically. Elastic scattering produces BSEs, where the incident electron is scattered by the nucleus of the atoms in the specimen. During inelastic scattering, kinetic energy can be transferred from the electron to the atom resulting in ejecting an electron, called secondary electron (SE) and generation of X-rays when the electron hole is filled by electrons at higher energy levels. The interaction volume for the electrons is pear-shaped beneath the surface as illustrated in Figure 2.8. The volume increases with the energy of the incident electrons in the probe. SEs comes from 5-50nm of the surface, while the BSEs from 50-300nm. The contrast formation can be divided into topographic and compositional contrast depending on the type of electrons contributing. SEs is the source of the topographic contract. This occurs from two effects i) variation in the surface depending on how the surface is oriented with respect to the detector ii) variation in number of electrons, since more electrons can escape from the edge. BSEs contribute to the compositional contrast, also called Z-contrast giving a variation in grey level. Higher atomic number generates more BSE making heavier elements appear brighter. This is very useful for a specimen with more than one chemical element.

The spatial resolution one can obtain in a scanning electron image relates to the electron signal detected (SE, BSE or transmitted), acceleration voltage, electron probe size and specimen thickness.

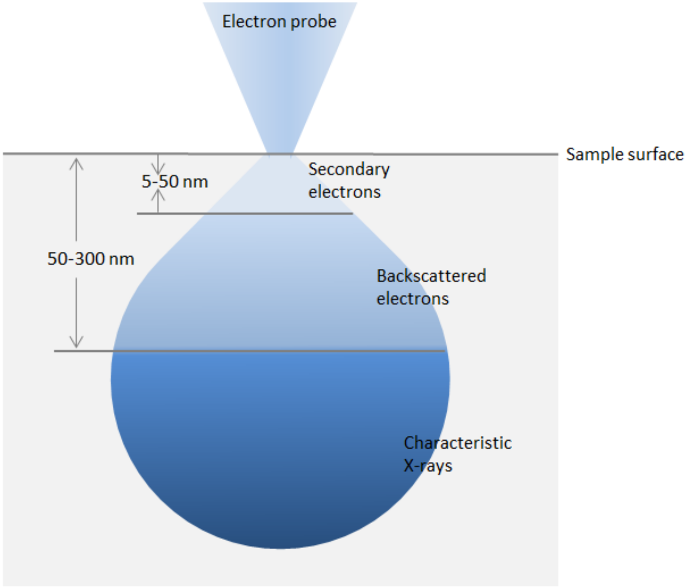

Figure 2.8: Secondary electrons, backscattered electrons and characteristic X-rays emitted from a volume below the surface is illustrated.

2.2.3 Transmission Electron Microscopy

Electrons are generally accelerated to 60-300kV. The beam goes through several electromagnetic lenses, whereas the lenses above the sample focuses the beam (de-magnifies the image of the filament) on the specimen and below in general magnifies and focuses either the image plane or back focal plane of the objective lens. Apertures are applied to control which electrons should be used making the image.

Images of the transmitted and forward scattered electron are in general shown at a fluorescence screen or detected by a CCD camera. When the beam hits the sample, different scattering processes occur. When inelastic scattering occur, the energy loss of the transmitted electrons can be detected by an electron energy loss spectrometer (EELS) located below the viewing screen while X-rays can be detected by an EDS detector above the sample.

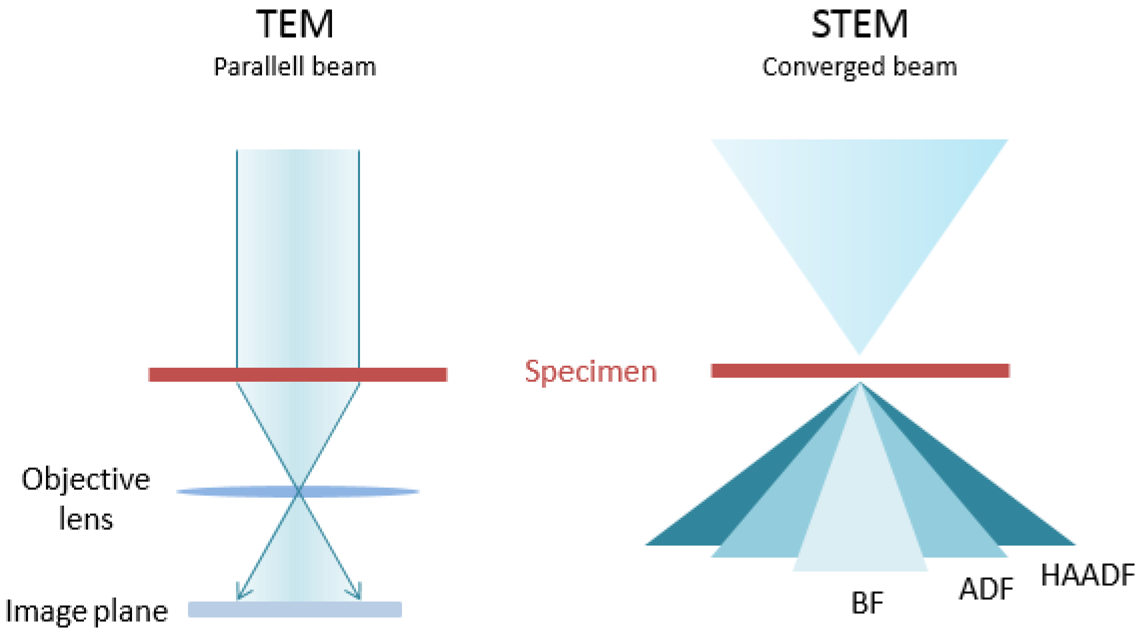

Figure 2.9: TEM with a parallel beam in image mode (right) and STEM with a converged beam diffracted beams at different angles (left).

2.2.4 Scanning Transmission Electron Microscopy

TEM can in operate in two modes: TEM or STEM (scanning transmission electron microscope) as illustrated in Figure 2.9. In TEM mode a parallel beam is used and either the direct or scattered beam gives a dark-field or bright-field image, respectively. While in STEM mode the incident beam is converged. Similar to TEM we choose between the scattered and unscattered beam. Annular detectors are placed below the sample to detect electrons scattered at different angles from the optical axis. An annular bright field detector collects unscattered electrons marked as *BF* in the figure. Electrons scattered with low angles ($<\sim 5^{o}$) are detected by an annular dark field (ADF) detector and at high angles ($>5^{o}$) by a high angle ADF (HAADF). For HAADF images amplitude contrast occurs, which arises from mass and/or thickness. The intensity of the beam depends on the atomic number only for HAADF, also called Z-contrast. Regions with high atomic number will scatter more electrons than regions with lower.

2.3 Powder X-ray Diffraction

Powder X-ray diffraction (PXD) is a widely used technique for analysis of inorganic crystalline materials. The theoretical and experimental aspects of the method is presented based on [20, 22].

2.3.1 Instrumentation

X-rays are electromagnetic waves generated by accelerating a beam of electrons onto a pure metal target contained in a vacuum tube. The process of generation of X-ray radiation is described in section 2.2.1. Generation of K_{α} and K_{β} radiation is from shell L to K, and $K_{\alpha1}$ and $K_{\alpha2}$ from subshell L_2 and L_3, respectively. In addition, a white radiation is emitted, called Bremsstrahlung. For a copper target, a nickel filter is used transmitting Cu K_{α} and not $K_{\beta.}$ Illustrated in Figure 2.10 is Bragg Brentano geometry for the instrumentation. Emitted X-rays interact with the sample and are scattered in an angle θ relative to the sample surface and collected by the detector. A slit is added to the X-ray tube to prevent divergence. By continuously changing the incident angle of the X-ray beam, a range of 2θ angles is recorded giving a diffraction pattern, assuming random orientation of the powder.

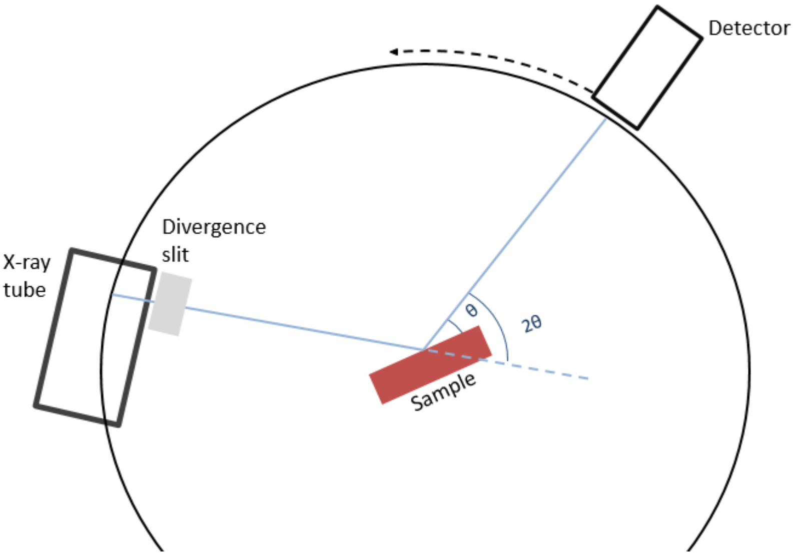

Figure 2.10: Demonstration of Bragg-Brentano geometrical arrangement of the source, specimen and detector.

2.3.2 Theoretical background

The distance between two parallel lattice planes is the lattice spacing, d. As illustrated in Figure 2.11, the angle of the incident X-ray, θ, is equal to the angle of the reflected X-ray. Diffracted X-rays interfere constructively when the total travel distance differs by an integer, we say they are in phase. If the X-rays have half an integer in difference, destructive interference occurs, we say they are out of phase. Constructive interference will occur when Bragg's law is satisfied:

$$n\lambda = 2d\, sin\, \theta \tag{5}$$

where n is an integer, λ is the wavelength, d is the spacing between the lattice planes and θ the angle of the incident beam relative to the sample surface. Each peak in a diffraction pattern represents a crystallographic plane. By taking positions into account, every crystalline substance has a unique pattern, like a fingerprint.

Several parameters affect the position, intensity and broadening of the Bragg peaks, whereas defects in crystal lattice, such as substitution will affect the d-spacing and thus the position.

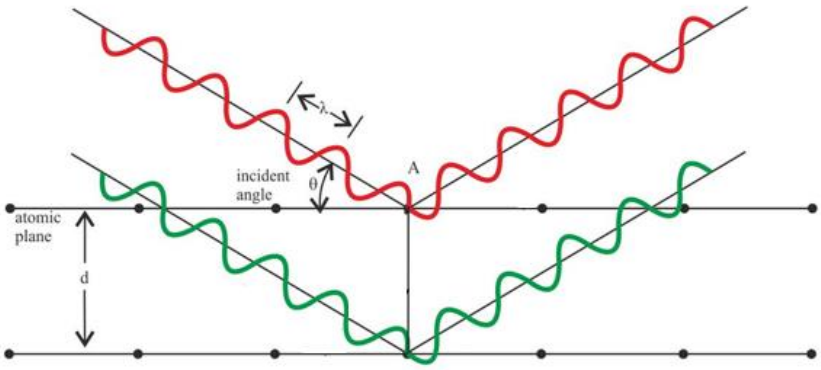

Figure 2.11: Bragg diffraction by crystal planes, modified from [23].

Ideally should Bragg reflections appear as sharp lines but in reality, a broadened peak is obtained. This is due to many factors such as instrumental errors, crystallites size and shape, and structural defects. This occurs more in a larger crystallite than a small, which is why the peaks width increases with decreasing crystals size, thus is the crystal size is inversely related to the peak width. However, structural defect can occur by residual stress causing strain due to compressing or stretching bonds between atoms, thus changes the spacing of the lattice planes.

2.4 Defect chemistry

This chapter is written as an introduction to defect chemistry based on [18].

At finite temperatures, all crystalline materials contain deviations from their periodic arrangement, called defects. Many properties of a material can be explained by the knowledge and understanding of its defect structure. The classification of the defects is done based on how many dimensions they effect:

- Zero-dimension defects, this is point defects affecting one lattice point such as; vacancies, substitution, interstitials and electronic defects.
- One dimension defects, this is line defects for instance dislocations
- Two dimensional defects are plane defects; stacking faults, grain boundaries and surfaces.
- Three dimensional defects, these are often volume defects; cracks, precipitates and foreign includes.

Kröger-Vink notation

Point defects can be described by the Kröger-Vink notation. The defect is described by A_s^q, where A is the chemical content, s is the structural position it occupies and q the effective charge with respect to a freely chosen reference state. For neutral charge *x* is used, while "•" and "'" is used for positive and negative charge, respectively. Interstitials are represented with *i* and vacancies with *v*.

Defects present in $Zn_{1-x}Al_xO$

Three main defects are expected for $Zn_{1-x}Al_xO$ i) Al substituting Zn ii) oxygen vacancies and (iii) electrons as charge carriers.

The incorporation of Al into the structure can be expressed as

$$\mathbf{Al_2O_3 + ZnO \rightarrow Zn_{Zn} + 2Al_{Zn}^{\bullet} + 3O_O^x + \frac{1}{2}O_2(g) + 2e'} \qquad (6)$$

While the formation of oxygen vacancies by

$$\mathbf{O_O^x = v_o^{\bullet\bullet} + 2e' + \frac{1}{2}O_{2(g)}} \qquad (7)$$

With $n = [e']$, the overall charge neutrality requires $n = [\mathrm{Al}_{\mathrm{Zn}}^{\bullet}] + [\mathrm{v}_{\mathrm{O}}^{\bullet\bullet}]$. All chemical reactions in equilibrium can be expressed by an equilibrium constant, K, providing a relationship between the reactants and products activity at a given temperature. By assuming oxygen vacancies and compensating electrons as the predominated defects, i.e. an intrinsic situation, the electro-neutrality condition simplifies to $n = 2[\mathrm{v}_{\mathrm{O}}^{\bullet\bullet}]$. The electron concentration thus depends on the oxygen partial pressure as

$$\mathbf{[n] = (2K_{v_O^{\bullet\bullet}})^{1/3}\, \boldsymbol{p}O_2^{-1/6}}. \qquad (8)$$

On the other hand, for a doped material, $n = [\mathrm{Al}_{\mathrm{Zn}}^{\bullet}] \gg [\mathrm{v}_{\mathrm{O}}^{\bullet\bullet}]$, so that the electron concentration is independent of the oxygen activity.

Other defects reported for ZnO are Zn vacancies and interstitials, but they are neglected here as they are only relevant under extremely oxidizing or reducing conditions [24, 25].

2.5 Electrical conductivity

This section is a brief introduction to the basic theory of electrical conductivity based on [26, 27].

The electrical conductivity describes the ability of a material to transport charge upon a potential gradient. Generally, the conductivity is directly proportional to the concentration of mobile charge carriers, c, and their mobility, μ. The electrical conductivity for electrons as the charge carriers is given by

$$\sigma = ne\mu_e \tag{9}$$

The latter can be related to relaxation of accelerated charge carriers by different scattering processes.

The electronic band structure of solids consists of energy states, whereas the valence band consists of the highest energy states filled with electrons and the conduction band energy states partly filled with electrons. These are the bands closest to the Fermi level, which is the upper most occupied energy state at absolute zero and the distance between the bands is called the band gap. Depending on the bandgap and thus the electronic properties solids can be categorized as a metal, semiconductor or insulator. Out of these, semiconductors offer the widest possibility to tune the properties of a material for a certain application and the following discussion will thus be limited to this class of materials. Many electronic properties of a semiconductor can be understood on basis of its electronic band structure and the position of the Fermi level with respect to the band gap. The charge carrier concentration of a semiconductor can be changed and controlled by introduction of foreign atoms into the material. It can either be doped with atoms that donate electrons to the conduction band or accept electrons from the valence band, resulting in n-type conductivity with electrons being the dominant charge carrier, or p-type with hole conductivity, respectively. If the doped carrier concentration is large, the Fermi level lies close or even within the band, and the transport properties are similar to a metal. This is called a degenerate semiconductor. With lower doping levels or increasing temperature, the Fermi level moves towards the middle of the band gap, the distribution function can be approximated by Boltzmann statistics and the material is called non-degenerate.

The mobility of charge carriers is determined by the scattering frequency with lattice vibrations or structural imperfections such as dislocations, grain boundaries and impurities. Typically, the scattering frequency of mobile charge carriers increases with increasing temperature, so that the mobility decreases. For a material with approximately constant carrier concentration, the conductivity thus decreases with increasing temperature. For a non-degenerate semiconductor, however, the carrier concentration increases exponentially with temperature due to thermal excitation across the band gap, effectively overcompensating the decrease in mobility.

2.6 Seebeck effect

The Seebeck effect describes the ability of a material to generate a voltage, when held under a temperature gradient. When two different sides of a material are kept at different temperatures, the charge carriers at the hot side will gain more energy and move towards the cold side faster than the opposite. This results in higher charge carrier concentration at the cold side causing a voltage difference over the sample. A material either can be *n*-type (negative charge carriers) or *p*-type (positive charge carriers). Figure 2.12 illustrate this process. The Seebeck coefficient relates the generated voltage to the temperature gradient:

$$\alpha = \lim_{\Delta T \to 0} \frac{U}{\Delta T} \qquad (10)$$

For a non-degenerate (Boltzmann statistics apply) *n*-type semiconductor, the Seebeck coeffient, α, is given by [26]

$$\alpha_e = -\left(\frac{k_B}{e}\right)\left[{}^{5}\!/_{2} - ln\left(\frac{N_c}{n}\right) + a_e\right] \qquad (11)$$

where N_c is the density of states in the conduction band, k_B the Boltzmann constant, *n* the concentration of mobile electrons and a_e (typically negligible) is correction terms for thermal collisions and related factors. The equation is analogous for electron holes as charge carriers.

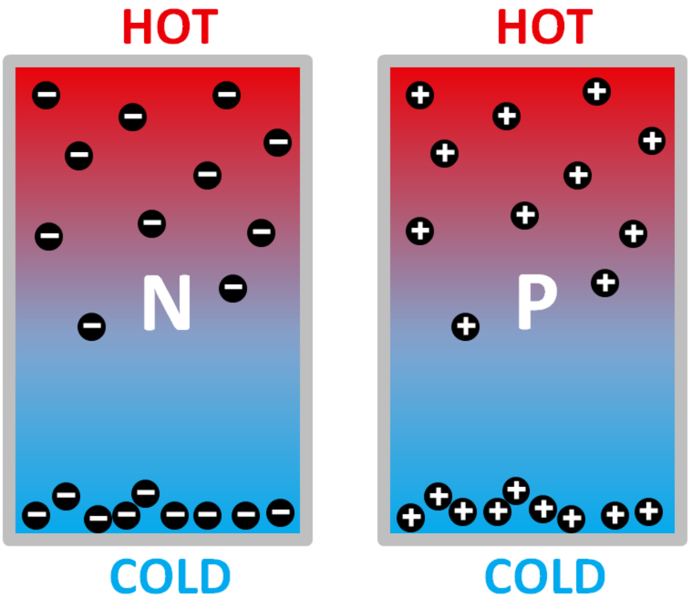

Figure 2.12: Illustration of n-and p-type semiconductors, where both sides of the material are exposed to different temperatures generating a potential difference.

By measuring the Seebeck coefficient, the voltage sign will indicate which type of charge carriers is dominant in the material. For an n-type semiconductor, the colder end will be negative with respect to the hot end and the Seebeck coefficient is negative. The same will happen for a p-type semiconductor, giving a positive Seebeck coefficient. For metals or degenerated semiconductors the Seebeck coefficient is given by [2]

$$\alpha = \frac{8\pi^2 k_B^2}{3eh^2} m^* T \left(\frac{\pi}{3n}\right)^{2/3} \tag{12}$$

where k_B is the Boltzmann constant, h is Planks constant and m^* is the effective mass.

2.7 Thermal conductivity

In this section a brief introduction to thermal conductivity will be given based on [27, 28].

Heat travels through a material from a hot side towards a cold as a flux. The heat transport in solids can be described as *Fourier's law* under steady state conditions by

$$j_U = -\kappa \frac{dT}{dx} \tag{13}$$

where j_U is the heat flux, κ the thermal conductivity and dT/dx is heat concentration gradient. The minus sign defines positive heat flow in the direction of decreasing temperature. Thermal energy transfer is a random process, suffering frequent collisions.

On a microscopic level, heat in a solid is transported by electrons or structural vibrations, phonons. If we assume that they are independent of each other, the thermal conductivity can be expressed as

$$\kappa = \kappa_e + \kappa_l \tag{14}$$

where κ_e is the electronic contribution and κ_l is the lattice contribution.

A useful characteristic temperature of a material is the Debye temperature, θ_D, which roughly corresponds to the temperature above which all possible phonon modes are populated.

Lattice contribution to thermal conductivity

The mean free path of phonon defines the scattering of the lattice contribution of the thermal conductivity. This is given by

$$\kappa_L = \frac{1}{3} C v l \tag{15}$$

where C is the heat capacity, v is the average particle velocity and l is the mean free path between collisions. At temperatures above the Debye temperature, C is estimated to be $3k_B$ for each atom in the unit cell, which is known as Dulong-Petit's rule.

Similar to electronic transport, also thermal conduction can be described by a relaxation time, reflecting the scattering of phonons. Phonons can be scattered by different scattering processes as phonon-phonon interactions, point defects, particles and grain boundaries, which all contribute to reducing the relaxation time.

The interatomic forces of atoms within the crystal can be approximated by a harmonic potential, where the restoring force is proportional to the atomic displacement. However, if the material consisted of only harmonic interactions, there would not be any collisions between different phonons and the mean free path will be limited by collisions of the phonon by crystal boundary and lattice imperfections. This can, for example, be observed at cryogenic temperatures, where the atomic displacements are small, the harmonic approximation holds and the thermal conductivity reaches very large values.

Phonon-phonon scattering can be described as

$$\boldsymbol{K_1} + \boldsymbol{K_2} = \boldsymbol{K_3} \tag{16}$$

where K_i are the wave vectors of the involved phonons. Two fundamentally different situations could occur:

(i) K_3 is within the first Brillouin zone as shown in Figure 2.13a. This is called a normal process (N-process). The two incoming phonons create one outgoing phonon and the total momentum of the phonon gas is not changed by the collision. N-processes do not contribute to the thermal resistivity directly, but lead to a redistribution of the phonon population, which makes it difficult to account for N-processes in theoretical calculations.

(ii) K_3 lies outside the 1. BZ, i.e. the corresponding phonon can be represented by a phonon within the 1.BZ, when replacing it by a reciprocal lattice vector G:

$$\boldsymbol{K_1} + \boldsymbol{K_2} = \boldsymbol{K_3} + \boldsymbol{G} \tag{17}$$

This is called an Umklapp process (U-process) and is shown in Figure 2.13b. The total momentum of the phonon gas has changed and U-processes thus contribute to the thermal resistivity of the solid.

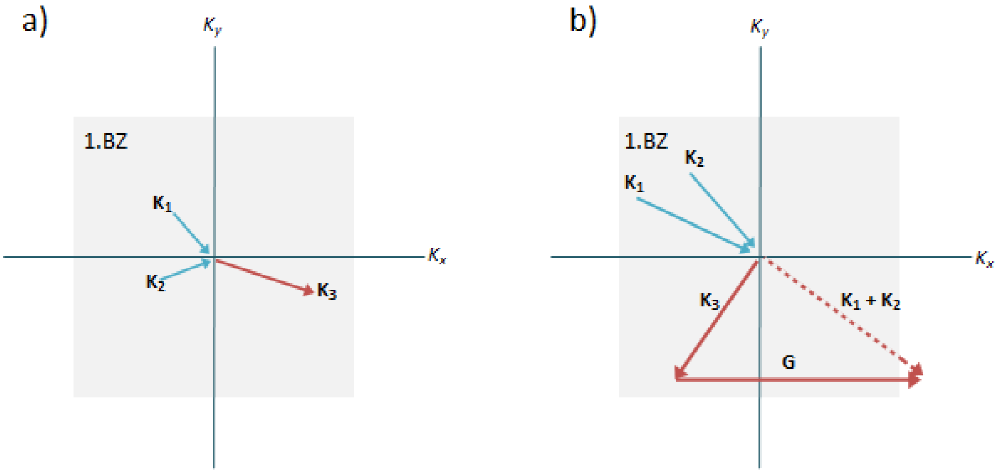

Figure 2.13: a) Normal process b) Umklapp process

Umklapp scattering is dominating at high temperatures (above Debye temperature) with T^{-1} dependency [27]. This is because the scattering rate of Umklapp processes increases with T [29]. At lower temperatures grain boundary and point-defect scattering are dominating.

Point defects and grain boundaries are deviations from the periodic crystal structure and will thus scatter phonons. In order to reduce the thermal conductivity for thermoelectric applications, it is thus desirable to increase phonon scattering. For example, in doped materials, an atom in the crystal structure is replaced by another with a different size and mass. This will act as an impurity and scatter. The larger mass and size difference the more scattering occurs. Other phonon engineering strategies include nanostructuring the material via precipitates or mechanical properties to enhance grain boundary scattering [30-34] or choosing complex crystal structures with large unit cells to enhance U-processes [2, 35-37].

Electronic contribution to the thermal conductivity

The electronic contribution to the thermal conductivity is related to the electronic conductivity via the Wiedemann-Franz law

$$\kappa_e = L_0 \sigma T \tag{18}$$

where L_0 is the Lorenz coefficient 2.45 x 10^{-8} W s^{-1} K^{-2} [28]. This assumption is valid for most metals and degenerated semiconductor above the Debye-temperature.

Chapter 3

Experimental methods

In this chapter, the experimental methods and parameters used in this thesis will be presented. Synthesis and preparation methods will be presented first, followed by the characterization techniques used for microstructural structural determination, such as SEM, TEM and XRD. In the end, measurement techniques for thermoelectric transport properties will be presented.

3.1 Sample synthesis

The samples investigated in this thesis were prepared by solid state and sol-gel synthesis methods. For the samples made using solid-state synthesis, two different ball milling techniques were applied; roll ball milling and planetary ball milling. Sol-gel samples are denoted *wc* (wet chemical), solid state synthesis with planetary ball milling *ssp* and solid state synthesis with roll ball milling, *ssr*. Three different compositions of ZnO was prepared for all synthesis routes; with 0, 1 and 5% Al content. 10 pellets were prepared with the same sintering conditions. In addition, two samples with the same composition were prepared at lower sintering temperatures.

3.1.2 Sample synthesis by sol-gel

Sol-gel samples were prepared from $Zn(NO_3)_2{\cdot}6H_2O$ and $Al(NO_3)_3{\cdot}9H_2O$ precursors listed in table 3.1. The synthesis route is described in the steps below:

1. **Weighing and mixing of precursors**. Stoichiometric amounts of $Zn(NO_3)_2{\cdot}6H_2O$ and $Al(NO_3)_3{\cdot}9H_2O$ were weighted with an analytical weight, Sartorios ED2245. The powders were mixed with calculated amounts of distillate water to obtain a 1M zinc solution. In addition were 5ml ethylene glycol added.

2. **Sol-and gel-formation**. The solution was heated to 80°C and kept for one hour. During that hour, arbitrary amount of citric acid was added, while mixed using a rotating

magnet. The amount of citric acid is unknown. The beaker with the solution was placed in a Heraeus heating cabinet at 100°C until the water had evaporated.

3. **Frist calcination**. The powder formed from the sol-gel mixture was lightly crushed using mortal and pistol, before added to a biker. The powder was calcinated in a Nabertherm LV 5/11/P330 furnace for calcination for 1 hour at 500°C with a ramp rate of 8.3°C/min.

4. **Second calcination**. A second calcination was performed due to uncomplete reactions, where the powder again was was lightly crushed using mortal and pistol, before placed in an alumina crucible at 900°C for 10 h with a ramp rate of 2.5°C/min. This was done in the same furnace as the previous step.

5. **Pellet pressing**. Approximately 1g of obtained powder was weighted out and mixed with a binder (B60/70 mixed with ethyl acetate) to prevent cracks, using 10 drops per gram. The powder was pressed into a pellet using a 13mm die and a Specac pellet press, pressed with ~1.5t.

6. **Sintering**. The pellets were sintered on a pile of sacrificial powder from the same batch, placed on an alumina plate with an alumina cover. The samples were sintered in a Nabertherm LHT 04/17 at 1500°C for 10h with ramp rate 4.16°C/min.

Chemical	Formula	Purity	Supplier
Zinc nitrate hexahydrate	$Zn(NO_3)_2 \cdot 6H_2O$	99.0%	Sigma-Aldrich
Aluminum nitrate hexahydrate	$Al(NO_3)_3 \cdot 9H_2O$	$\geq$ 98	Sigma-Aldrich
Ethylene glycol	$C_2H_6O_2$	99%	Alfa Aesar
Citric acid	$C_6H_8O_7$	$\geq$ 99.5%	Sigma-Aldrich

Table 3.1: Precursor materials used for synthesis of sol-gel samples.

3.2.2 Sample synthesis by solid state synthesis

Solid state samples were prepared from ZnO and Al_2O_3 precursor listed in table 3.2. As mentioned, two different ball milling techniques was used. The steps for both methods will be presented below. Step 2a corresponds to planetary ball milling and 2b to roll ball milling.

1. **Weighing**. Stoichiometric amounts of ZnO and γ-Al_2O_3 were weighted with an analytical weight, Sartorios ED224.

2.a **Planetary ball milling**. The weighted powder, spherical agate balls and isopropanol was added to an agate jar. The balls had a diameter of ~10mm and approximately half of the jar was filled with isopropanol. A Retsch PM100 rotary mill was used at 300rmp for 2 hours with 15 min intervals. After milling the powder was dried at ~100^{o}C in a Heraeus heating cabinet at 100^{o}C until the isopropanol had evaporated.

2.b **Roll ball milling**. The weighted powder, cylindrical zirconia balls and isopropanol was added to a polyethylene bottle. The cylindrical balls had ~10 mm diameter and height and approximately ¾ of the jar was filled with isopropanol. A Ball Mill Model 12VS mill was used at approximately half of the maximum speed for 24 hours. After milling the powder was dried at ~100^{o}C in a Heraeus heating cabinet at 100^{o}C until the isopropanol had evaporated.

The powders were then pressed and sintered in similar manner as for sol-gel in section 3.1.2.

Exceptions: In addition to the samples prepared by the above descriptions, two pellets from the batch 1ssp were sintered at 1200°C and 1350°C, with the same sintering time and ramp as the others, to investigate influence of sintering temperature on transport properties.

Chemical	Formula	Purity	Supplier
Zinc oxide	ZnO	99.99%	Sigma-Aldrich
Aluminum oxide	γ-Al_2O_3		Merck

Table 3.2: Precursors used for samples prepared by solid-state synthesis

3.2 Density measurements

Density of all samples was measured with Archimedes density using a density determination kit ,Sartorius YDK03, with water as the immersion liquid of choice. The density was measured dry, m_{dry}, and immersed, m_{im} and the density was obtained from the following relation

$$\rho_A = \frac{m_{dry}\rho_{liq}}{m_{dry} - m_{im}} \tag{19}$$

where p_{liq} is the density of the water at room temperature. The relative density of all samples was calculated based on the theoretical density of ZnO of 5.61 g/cm^3. This value is not accurate due to substitution and presence of precipitates (with lower density 4.61 g/cm^3) not taken into account. The relative density is therefore only calculated for comparison with reported values.

3.3 Powder X-ray Diffraction

PXD measurements of all samples were carried out with a Rigaku MiniFlex600 diffractometer (CuK$_\alpha$), equipped with a D/teX Ultra High speed 1D detector. Data were collected in the range of 20^o - 90^o 2θ (Bragg-Brentano geometry), with a step size of 0.02^o. Prior measurements a small amount of Si (NIST 640d), which acted as an internal standard, was added to all samples. Quantitative phase analysis of the obtained PXD patterns was performed with the Diffract software combined with the Powder Diffraction File (PDF) database. To calculate unit cell parameters of formed phases, selected PXD patterns were analysed by the La Bail refinement (profile matching) with the Fullprof Suite program.

3.4 Scanning Electron Microscopy

The microstructure of sintered samples was investigated with a Hitachi TM300-Tabletop, with a tungsten filament and backscattered electron detector. The microscope was operated in vacuum with an acceleration voltage of 15 kV. Energy dispersive X-ray spectroscopy (EDS) was used for the characterization of the chemical composition of the samples. The EDS spectrometer and the analysis software are a part of the Quantax70 series delivered by Bruker. The samples were mounted on an aluminium stub with a carbon tape for SEM investigations

SEM specimen preparation

Two series of samples were prepared for microstructural analysis. To investigate the cross section, the fractured pellets was casted in demotec33. The sample was grinded with SiC papers with particle size of 15 μm on the final paper. Polishing was done on final MD–nap with 1 μm diamonds and with green DP-lubricant provided by Struts.

To investigate the grain size, the sample surface was polished with SiC paper with grain size of 5 μm on the final paper. The samples were then thermally etched in a Nabertherm LHT 04/17 furnace at 1200ºC for 40 min with ramp rate 6.6ºC/min.

3.5 Scanning Transmission Electron Microscopy

STEM images were acquired on two microscopes in this thesis:

(i) **JEOL JEM-2100F, operated at 200kV.** The instrument is equipped with a Schottky FEG and a pole piece giving a point resolution of 1.9 Å. Images were acquired with an EM-24541SI0D Annular Dark Field detector and EDS spectra by an Oxford instrument X-Max^{N} 80 T, with a Silicon Drift Detector (SDD). STEM-EDS was performed with a scanning probe of 1 nm. The EDS experiments were done with k-factors; k_{Zn} = 1.322, k_{Al} = 1.046 and k_{O} = 2.003 and the data was analysed by AZtecEnergy software provided by Oxford Instruments.

(ii) **FEI TITAN G2 operated at 60-300**. The instrument is equipped with spherical aberration probe corrector giving a spatial resolution of 0.8Å. The EDS spectra was collected by a Super-X EDS detector with k-factors; k_{Zn} = 1.895, k_{Al} = 1.002 and k_{O} = 1.240 and the data was analysed by software Esprit 19.

TEM specimen preparation

TEM wedge specimens were prepared by mechanical grinding. The specimen was first grinded with SiC paper to a thickness of ~150 μm and then further thinned and polished using a MultiPrep machine. Diamond lapping films with particle sizes from 30μm to 1μm was used. The final thinning was done by ion milling with a Gatan PIPS model 695 or PIPS II. The thinning steps used were as follows; upper and lower source voltage 5keV with milling angle 8° for 20 min, followed by 3 keV with 7° for 10min, 1 keV with 6° for 5 min and 0.5 keV with 5° for 5 min. The sample was then mounted on a Cu ring using glue from the Gatan cross-sectional kit (MODEL 601.07).

3.6 Electrical conductivity and Seebeck coefficient measurements

The electrical conductivity and Seebeck measurements were performed in Probostat measurement cell manufactured by NorECs AS. The cell consists The cell was gas-tightly closed with a quartz tube before placed in a vertical tubular furnace which provides the base temperature of the measurement. The cell is flushed with a chosen gas composition and controlled by an in-house built gas mixer. The sample setup is illustrated in Figure 3.1, where the sample is placed on top of the alumina support tube supported with a spring load system. The setup consists of three thermocouples, whereas two of them are S-type (Pt-Rh10. Pt) placed in contact with the sample illustrated as top and bottom thermocouple in Figure 3.1. The Pt-leads of the thermocouple acts as temperature and voltage probes to measure the induced thermoelectric voltage across the sample.

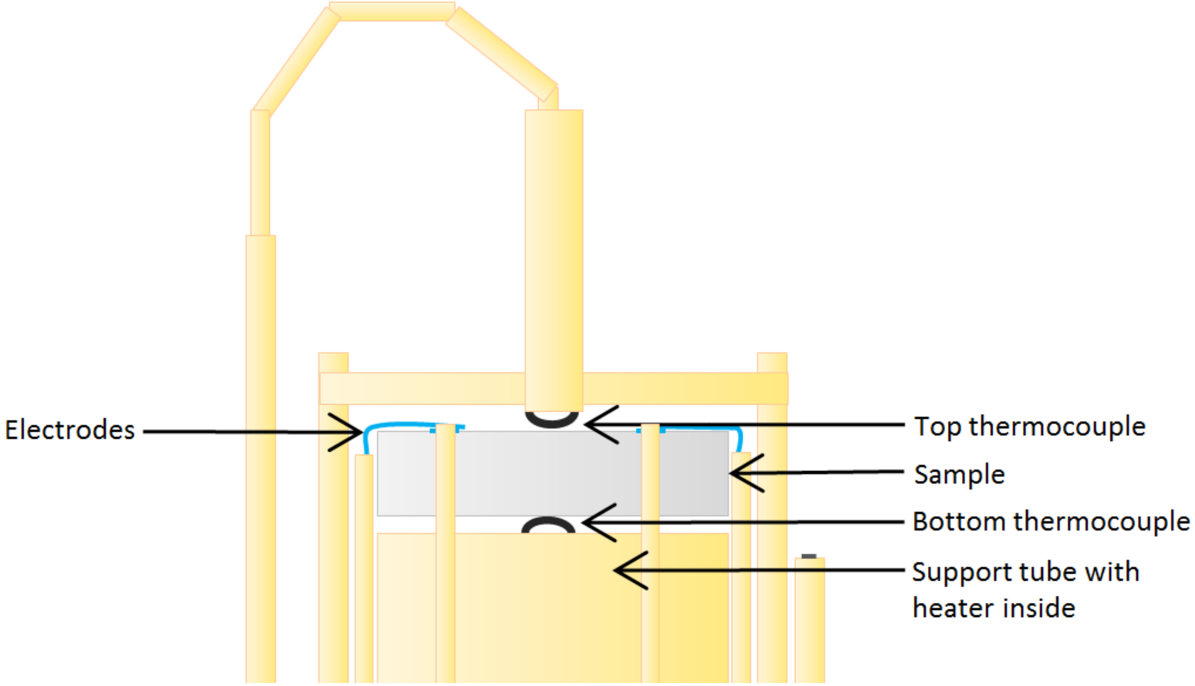

Figure 3.1: Schematic figure of the measurement cell showing how the sample is situated.

The thermoelectric voltages is induced when a temperature gradient is applied across the sample by coils of P110Rh with temperature resistance of ~5Ω, placed inside the support tube, underneath the. A third thermocouple is placed outside of the support tube to control the base temperature of the furnace. In addition, four Pt electrodes placed on the sample surface, held in position by a spring-load system, act as voltage and current probes for the van der Pauw measurements. The measurements are controlled and recorded by an in-house made LabVIEW program [38].

Gas mixer

The atmosphere under which the measurement is performed, is set and controlled by gas mixers. In this thesis a mix of two gasses, G1 an active gas (O_2) and G2 an inactive gas (Ar) was used. In the first step G1 will be diluted with G2 to create a mixture. The obtained mixture can be diluted a second time using G2 if desired. The gas will further either be dried or humidified. . In this project only dried gas was used which were dried by passing the gas through phosphorous pentoxide (P_2O_5) powder. The gas then flows to the Probostate, where the amount is controlled by flowmeters. The excess of each mixture is bubbled into a column of dibutyl phthalate (B1-B3) to provide a constant pressure in the system [39].

Measurements conditions

Two different measurement conditions were applied when investigating the electrical conductivity and Seebeck coefficient, as follows:

(i) The temperature dependency of the electrical conductivity and Seebeck coefficient was measured from room temperature up to 850°C with 100°C intervals. Either no gas or a continuous flow of O_2 was applied during the measurement.

(ii) The influence of oxygen partial pressure on the electrical conductivity and Seebeck coefficient was measured by applying different concentrations of O2. The measurement was done after chemical steady state was reached, ensured by monitoring the electrical conductivity. Both the electrical conductivity and Seebeck coefficient was investigated under dried conditions in Ar (10 ppm O_2), 1% O_2, 10% O_2, and 100% O_2 at 850°C.

3.7 Thermal conductivity

To determine the thermal conductivity of the samples, the thermal diffusivity was measured using a Laser Flash Analysis (LFA) on a Netzsch LFA457 microflash.

A heat pulse is applied to the bottom of a sample coated by a graphite spray (GRAPHIT from Kontakt Chemie) to ensure absorption of the laser pulse. An infrared detector record the heat increase on the top side of the sample as a function of time, illustrated in Figure 3.2. The thermal diffusivity of the sample is then found through the following equation

$$D = \frac{1.38d^2}{\pi^2 \tau_{1/2}} \tag{20}$$

where d is the thickness of the sample and $\tau_{½}$ is the time required for the surface of the sample to reach half of the maximum temperature rise [40].

The heat capacity, C_p, of the sample is found through the reference sample Pyroceram 9606, provided by Netzsch, by applying a Cape-Lehman model fit to the diffusivity. The thermal conductivity can then be found from the following relation

$$\kappa = D\rho C_p \tag{21}$$

where ρ is the density of the current sample.

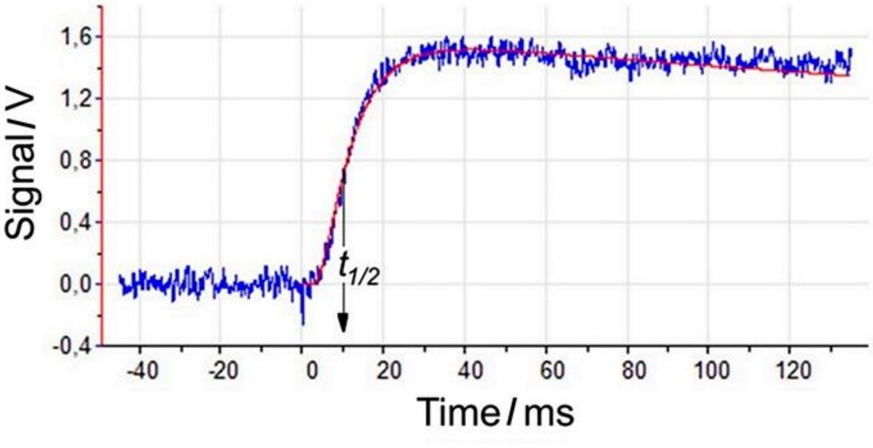

Figure 3.2: Signal vs time plot from a standard LFA measurement [40].

Chapter 4

Results

The presentation of the results will be structured by the different synthesis methods. The morphology of samples of each method has been characterized by XRD, SEM and TEM. In addition, the Seebeck coefficient, the electrical and the thermal conductivity are measured as a function of temperature to study the thermoelectric properties of the samples. Thermoelectrical measurements done for sol-gel (wc) are presented in green, solid-state synthesis with planetary ball milling (ssp) in blue and solid-state synthesis with roll ball (ssr) milling in pink. Circle symbols is used for ZnO, square for ZnO with 1% Al and triangle for 5% Al. Darker marker colours are chosen to indicate a higher nominal Al concentration. The sample ID x_yy_zz contains the nominal Al concentration x, the synthesis method yy, and, when different from 1500°C, the sintering temperature zz. All samples are listed in Table 4.1 with sample ID, composition, synthesis method and sintering temperature.

Sample ID	Nominal composition	Synthesis method	Sintering temperature [^{o}C]
Batch 1			
ZnO_wc	ZnO	WC	1500
1wc	$Zn_{0.99}Al_{0.01}O$	WC	1500
5wc	$Zn_{0.95}Al_{0.05}O$	WC	1500
ZnO_ssp	ZnO	SSP	1500
1ssp_1200	$Zn_{0.99}Al_{0.01}O$	SSP	1200
1ssp_1350	$Zn_{0.99}Al_{0.01}O$	SSP	1350
1ssp	$Zn_{0.99}Al_{0.01}O$	SSP	1500
5ssp	$Zn_{0.95}Al_{0.05}O$	SSP	1500
ZnO_ssr	ZnO	SSR	1500
1ssr	$Zn_{0.99}Al_{0.01}O$	SSR	1500
5ssr	$Zn_{0.95}Al_{0.05}O$	SSR	1500
Batch 2			
1ssr_b2	$Zn_{0.99}Al_{0.01}O$	SSR	1500

Table 4.1: Overview of all synthesized samples with sample ID, nominal composition, synthesis method and sintering temperature.

4.1 Sol-gel

4.1.1 Colour and density

Figure 4.1: Samples prepared by sol-gel, ZnO_wc (left), 1wc (middle) and 5wc (right), are shown to illustrate the colour difference .

An image taken of all samples prepared by sol-gel is presented in Figure 4.1. A light grey colour is observed for 1wc and 5wc, while ZnO_wc has a warm green colour. The difference in colour between samples with and without Al could be due to unintentional impurities of different kind for the different samples or to the presence of the secondary phase.

Table 4.2 gives an overview of the gravimetric density measured for all sol-gel samples by the Archimedes method. All samples had a relative density below 90 %, indicating a porous microstructure, in particular bearing in mind that only open pores would be filled with water and not internal pores. For the 1wc composition, different samples were used for different measurement techniques to obtain a close to as-sintered starting condition, where *el* corresponds to samples used for electrical and Seebeck measurements, and *therm* for thermal conductivity measurements. The difference between the 1wc_el and 1wc_therm sample illustrates poor repeatability, when sintering the same composition twice. However, it should be noted that the density measurement of each individual sample is highly accurate and repeatable.

Sample	Gravimetric density [g cm^{-3}]	Relative density
ZnO_wc	4.97	89%
1wc el	4.25	76%
1wc therm	5.01	89%
5wc el+therm	4.64	83%

Table 4.2: Density measured by Archimedes method for sol-gel samples.

4.1.2 Phase analysis and lattice parameters by powder XRD

In Figure 4.2 powder XRD diffractograms of all samples prepared by sol-gel synthesis, both before and after sintering, are presented. Samples labelled *before sintering* are taken after calcination at 900°C whereas samples marked *after sintering* are taken the as sintered samples (1500°C in air). The positions of the reflections and the intensity profile of the patterns were used to identify the phases present in the samples. It was found that all samples have peaks corresponding to hexagonal ZnO (marked with bullets) with Wurtzite type structure with space group $P6_3mc$ (card nr PDF 010708070 with a = 3.249 Å and c = 5.205 Å). However, for the 5wc samples a second set of reflections is evident (marked with diamonds) and these were found to be consistent with the cubic $ZnAl_2O_4$ phase with a spinel type of structure with space group *Fd3m* (card no. PDF 010708181 with a= 8.091 Å).

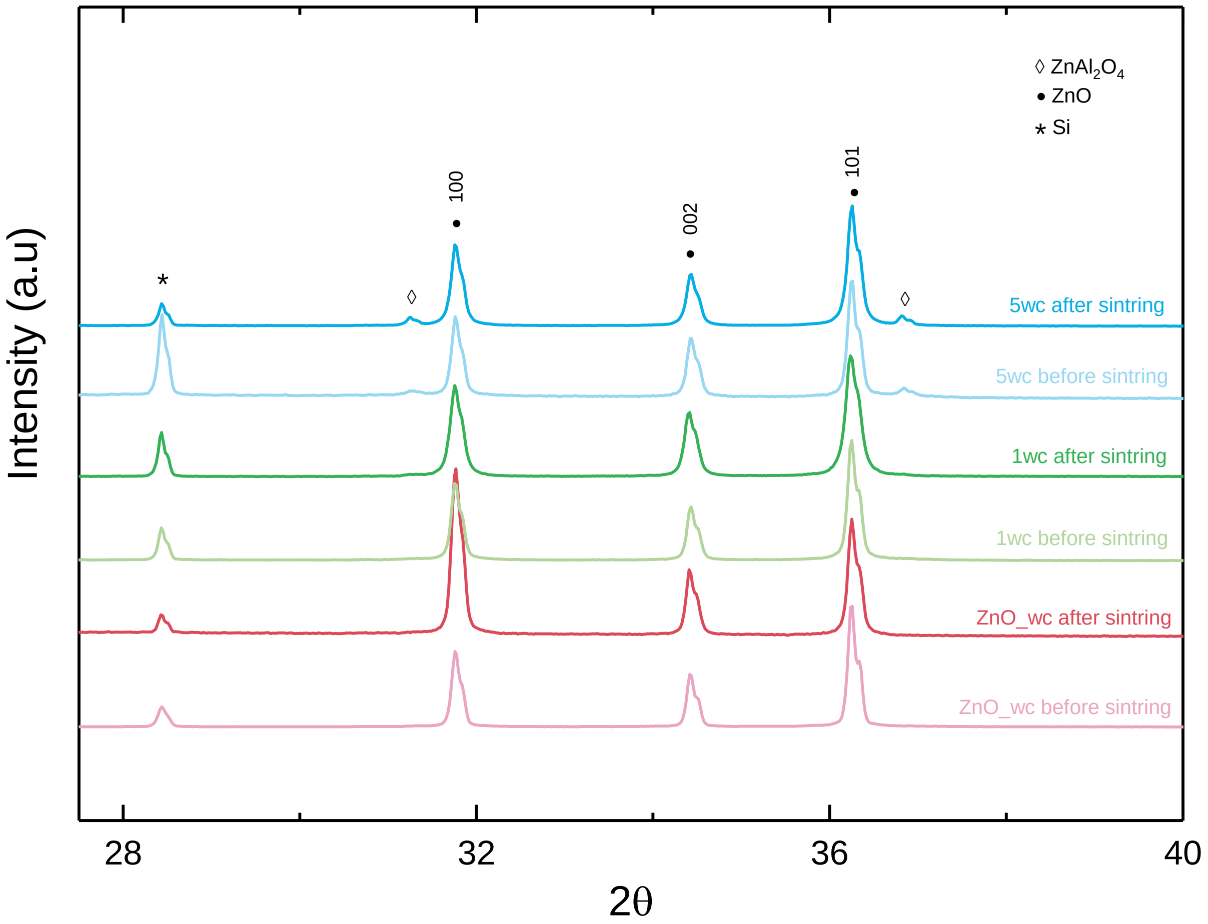

Figure 4.2: Powder XRD diffractograms from all the samples (0, 1 and 5 mol % Al) prepared by sol-gel synthesis before (brighter pattern) and after sintering (darker pattern) showing strong diffraction peaks from ZnO in addition to evident weaker peaks from $ZnAl_2O_4$ in the samples with 5 mol % Al. '*' represents preaks from the added Si standard.

In Figure 4.3 the resulting lattice parameters ‘a’ (black squares) and ‘c’ (green squares) are shown as a function of the Al concentration with their respectively values on Y-axis on the left and right hand. Compared to the pure ZnO specimen, the addition of 1 mol % Al increase both lattice parameters ‘a’ and ‘c’. The sample with 5 mol% Al is found to have similar ‘a’ lattice parameter as the 1 mol% Al doped specimen but it is found to have a c-axis with similar size as the pure ZnO reference sample.

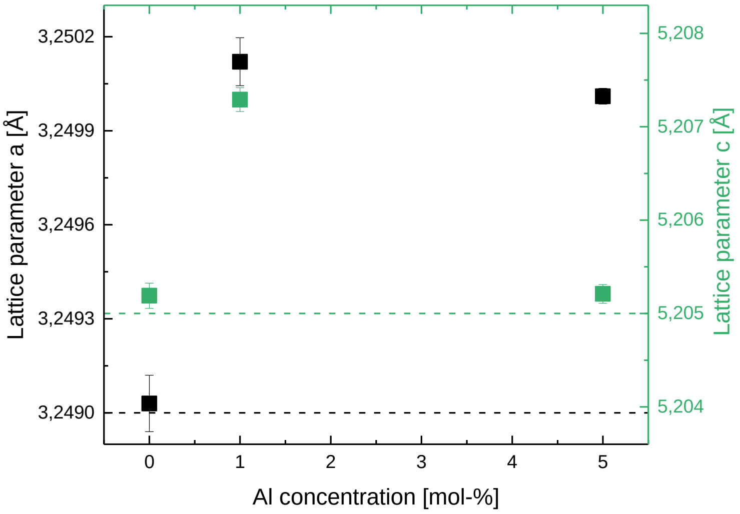

Figure 4.3: a) Lattice parameters ‘a’ and ‘c’ of ZnO after sintering determined by powder XRD as a function of Al concentration (mol-%). Black and green symbols correspond to the lattice parameter ‘a’ and ‘c’, respectively. Dashed lines indicate lattice parameters from PDF 010708070.

4.1.3 Investigation on microstructure by SEM

To investigate the influence of Al content on the microstructure of all the sintered sol-gel prepared samples, polished and etched (1wc), were studied by SEM. A summary of the results is shown in Figure 4.4, where the images are obtained using backscattered electrons and recorded with the same magnification in order to enhance the Z-contrast and enable direct comparisons between the samples a) ZnO_wc, b) 1wc and c) 5wc. Consistent with the XRD results the reference sample shown in a) is single phase ZnO. The darker areas seen are due to topography and pores in particular. In contrast what was evident from the XRD data $ZnAl_2O_4$,is found in both the 1 mol% and 5 mol% Al samples as shown in Figure 4.4b) and c) respectively where ZnO is consistent with the brighter areas (matrix) and $ZnAl_2O_4$ the darker particles (marked with blue rings). Black areas correspond to pores and carbon contamination as seen in the reference specimen. Comparing the microstructure of the 1wc and 5wc specimen it has been found that the specimen with 1 mol% Al content results in a homogenous distribution of the $ZnAl_2O_4$ particle, while the 5wc sample show some accumulated areas of the particle as illustrated in c). The increased Al content in the 5wc specimen compared to the 1wc is found to be correlated with a higher concentration of the $ZnAl_2O_4$ particles.

As grains are not evident on the polished specimens 1wc was thermally etched. As illustrated in Figure 4.4d, $ZnAl_2O_4$ particles are seen both at grain boundaries and inside grains of ~30µm (estimated by eye).

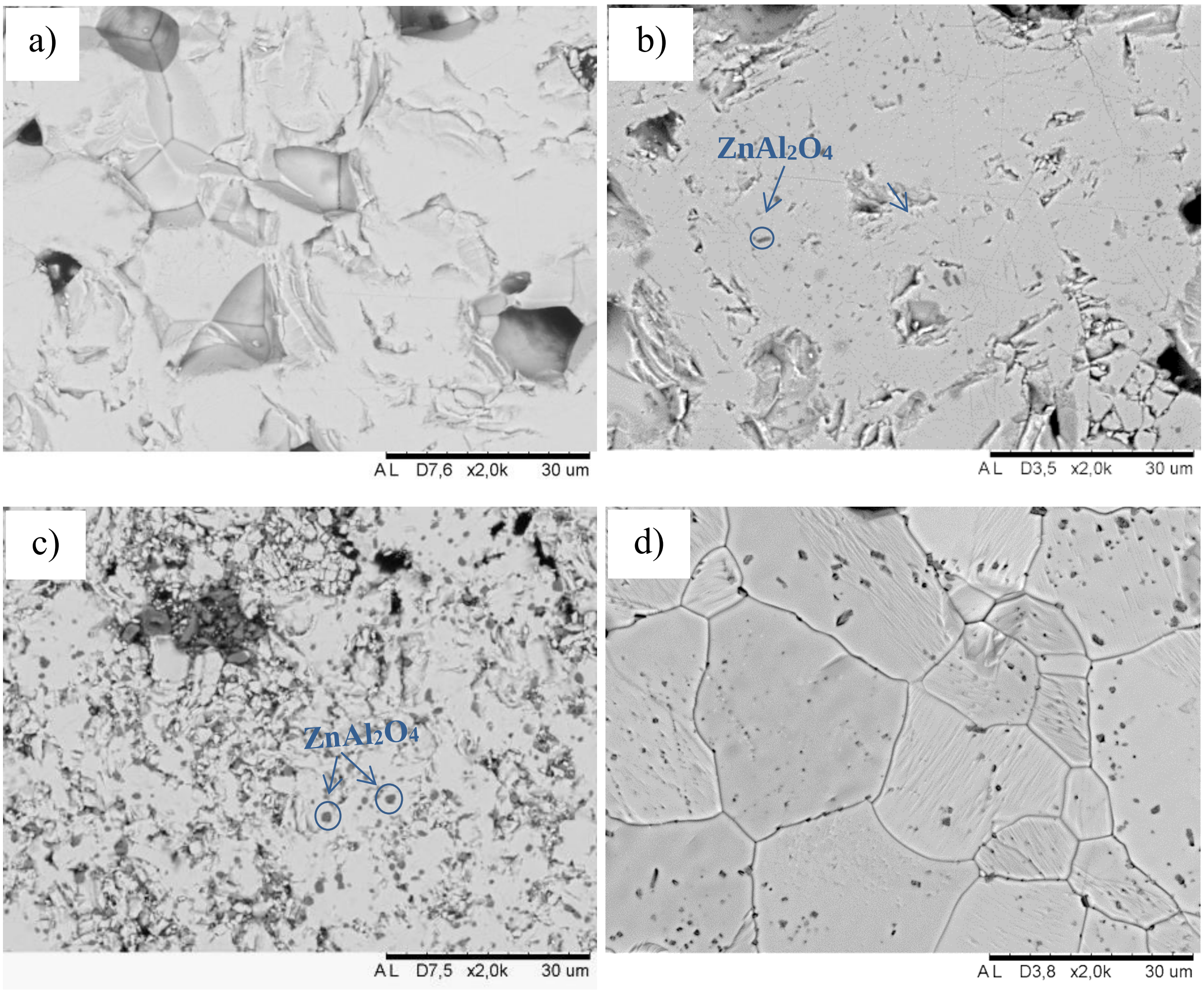

Figure 4.4: SEM images obtained from polished cross-section for a) ZnO b) 1wc c) 5wc. d) Shows thermal etched 1wc. Dark grey areas corresponds to particles of $ZnAl_2O_4$ and black to pores. The thermally etched sample shows homogenous distribution of $ZnAl_2O_4$ particles.

4.1.4 Electrical conductivity measurements

The electrical conductivity of 1wc (square) and 5wc (triangle) measured from 25°C to 850°C in air is presented in Figure 4.5a with arrows indicating the measurement start. From room temperature till 700°C, the conductivity is below 1 Scm^{-1} and after reaching 700°C it increases significantly, reaching values of ca. 3 Scm^{-1} and 5 Scm^{-1} for 5wc and 1wc, respectively. There is no clear trend with the Al content since 1wc has higher conductivity below 700°C and 5wc after 700°C. The influence of Al doesn't seem to be significant and trends could therefore be explained by other factors as impurity or density.

Oxygen partial pressure dependency was measured for 5wc at 850°C as shown in Figure 4.5b. Measurements were performed after chemical steady state was reached under dried conditions in Ar (10 ppm O_2), 1% O_2, 10% O_2, and 100%. Electrical conductivity changes with different atmospheres, whereas oxygen deficiency gave increase in electrical conductivity indicating an increase in oxygen vacancies from equation 8.

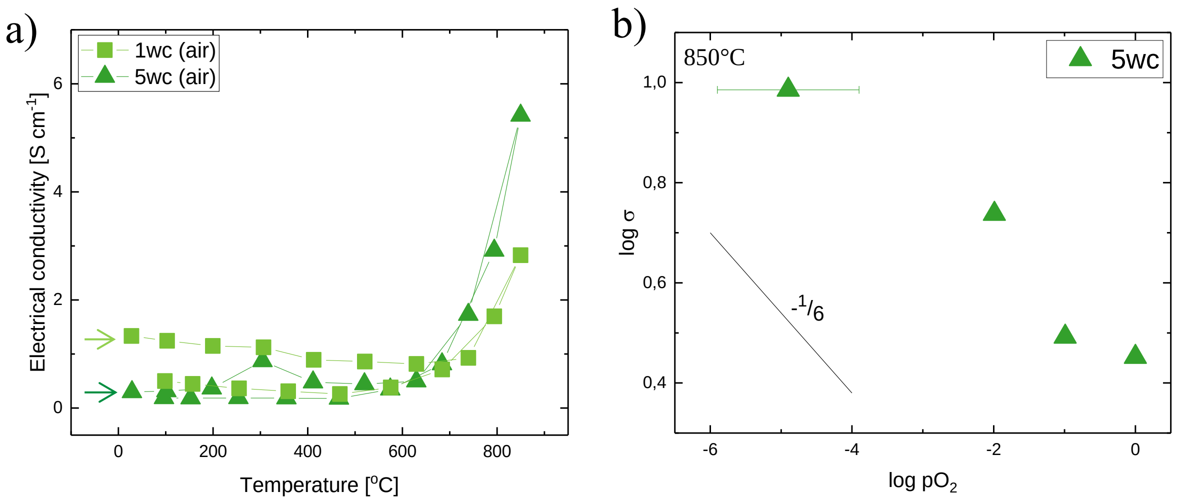

Figure 4.5: a) Electrical conductivity, σ, as a function of temperature for 1wc and 5wc. b) σ as a function of oxygen partial pressure for 5wc. Error bars are mostly relevant for measurements in Ar, due to higher sensitivity of leakage.. Slope of -$^1/_6$ indicates pO_2-depency for oxygen vacancies as dominating defect.

4.1.5 Seebeck measurements

Simultaneous with the electrical conductivity, also the Seebeck coefficient was measured for 1wc (square) and 5wc (triangle), Figure 4.6a. The Seebeck coefficient for both samples has negative values in the entire temperature range, indicating n-type conduction. α of both samples follow the same temperature dependence: Its absolute value increases with temperature. During cooling, the Seebeck coefficient of both samples is less temperature dependent and shows higher absolute values than during heating. The Seebeck coefficient is less dependent on microstructure or presence of secondary phases, but highly sensitive to the charge carrier concentration, with lower absolute Seebeck coefficient indicating a higher charge carrier concentration. Thus, the measurements show lower charge carrier concentration at the end of the measurement, than the beginning, in agreement with the reduced values of the electrical conductivity,

Figure 4.5a. The α values of 1wc and 5wc are fairly similar, but following the previous discussion, one may conclude that the latter has a lower carrier concentration.

pO_2-dependecy of Seebeck coefficient measured for 5wc is shown in Figure 4.6b. The measurements were done at identical conditions as the electrical conductivity measurements in Figure 4.5b. In agreement with the results for σ, we also observe a change of α by changing the atmosphere

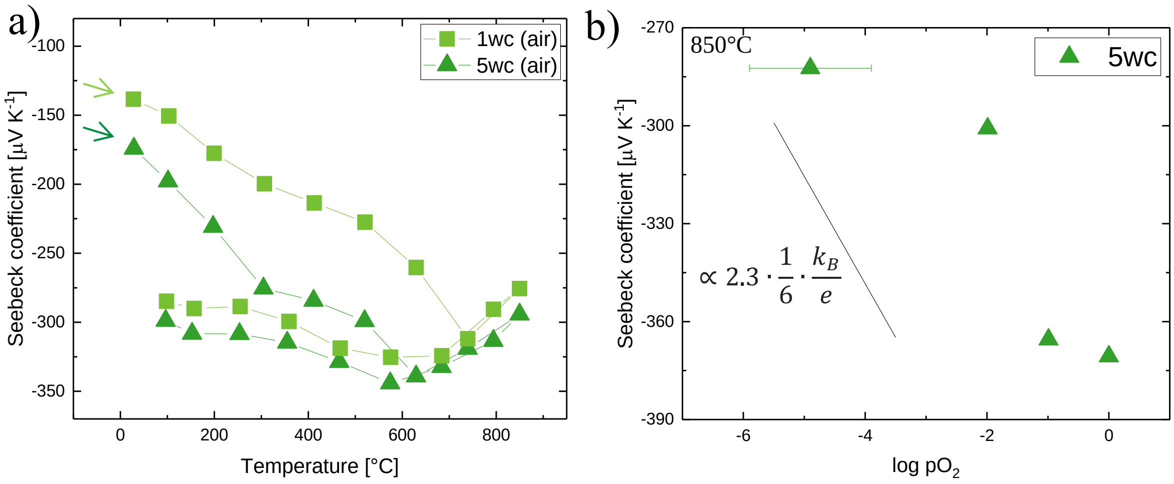

$\propto 2.3 \cdot \frac{1}{6} \cdot \frac{k_B}{e}$

Figure 4.6: a) Seebeck coefficient as a function of temperature for 1wc and 5wc. b) Seebeck coefficient as a function of oxygen partial pressure for 5wc. Error bars are mostly relevant for measurements in Ar, due to higher sensitivity of leakage. The slope indicates pO_2-depency for oxygen vacancies as dominating defect and is proportional to the slope of -1/6 for σ.

4.1.6 Thermal conductivity measurements

Thermal diffusivity was measured with the Laser Flash technique and the thermal conductivity was calculated from the results. The thermal conductivity measured for 1wc (square) and 5wc (triangle) as a function of temperature is presented in Figure 4.7 with arrows indicating the start of the measurement. Measurements were done from 50°C to 800°C with 100°C interval. Both samples have decreasing thermal conductivity with increasing temperature and a small spilt while cooling. 5wc has higher thermal conductivity and the difference between the samples is 20 W $m^{-1}K^{-1}$ at room temperature and decreases to 3.8 W $m^{-1}K^{-1}$ at higher temperature.

Because of the low values of the electrical conductivity, the electronic part to the thermal conductivity is negligible and not discussed for the sol-gel samples.

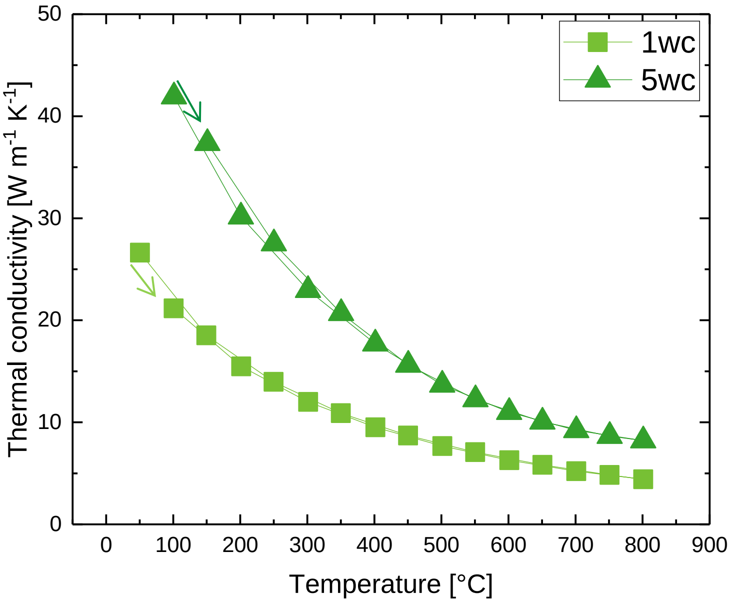

Figure 4.7: Thermal conductivity as a function of temperature for 1wc (square) and 5wc (triangle).

4.2 Solid state synthesis by planetary ball milling

4.2.1 Colour and density

Figure 4.8: Samples prepared by solid-state synthesis with planetary ball milling shown the colour difference, ZnO_ssp (left): yellow/brown, 1ssp (middle): green and 5ssp (right): grey.

As seen from Figure 4.8, the colour of the sintered pellets by solid-state synthesis with planetary ball milling (ssp) differs. The undoped specimens has a yellow-brown colour, while the 1ssp and 5ssp are greenish and grey, respectively. Some variation in shade can also be seen within a sample. In particular, the 1ssp specimen, showing brighter and darker regions. This could be due to density difference in the specimens. The difference in colour between the samples could be due to difference in density and amount of secondary phase present, and unintentional impurities of different kind.

During sintering, the samples with Al ended up with a white surface layer. This was polished away, but some remains can be seen at the rim of the 5ssp pellet in Figure 4.8.

Table 4.3 gives an overview of the gravimetric density measured for all ssp samples. Almost all samples had a relative density above 90 % and no obvious trend is observed.

Sample	Gravimetric density [g/cm^3]	Relative density
ZnO_ssp el	5.17	92%
ZnO_ssp term	5.34	95%
1ssp el	5.40	96%
1ssp term	5.30	94%
5ssp el	5.33	95%
5ssp term	4.77	85%

Table 4.3: Gravimetric and relative density measured for all samples prepared by ssp.

4.2.2 Phase analysis and lattice parameters by powder XRD

In Figure 4.9 powder XRD diffractograms obtained of all samples prepared by ssp, both before and after sintering, are presented. Samples labelled *before sintering* are taken after ball milling whereas samples marked *after sintering* are taken on the as sintered samples. It was found that all samples have peaks corresponding to hexagonal ZnO with Wurtzite type structure. However, for the 5ssp sample a second set of reflections is evident (marked with diamonds) and these were found to be consistent with the cubic $ZnAl_2O_4$ phase with a spinel type of structure. Shoulders shown on the right side of the reflection are due to the used Cu radiation source not been monochromated. 1ssp has an additional peak at 35^o, which is not visible due to the range in the figure. No peaks were detected for Al_2O_3 from the starting material, which indicates that all has been incorporated into the structure or formed the secondary phase. Comparing peaks after sintering, a peak broadning is observed with increasing al content, indicating a smaller grain size with increasing amout Al.

Figure 4.10a shows the obtained lattice parameters as a function of the Al concentration for as-sintered samples. Increasing amount of Al shows a decrease of both lattice parameters. Which is expected since Al^{3+} has a smaller ionic radii than Zn^{2+}. However, the undoped ZnO has larger lattice parameter than the values from the PDF card. The reason for this is unclear. The ratio between the lattice parameter varies for the different Al content, which could indicate stress/strain affecting the lattice planes different.

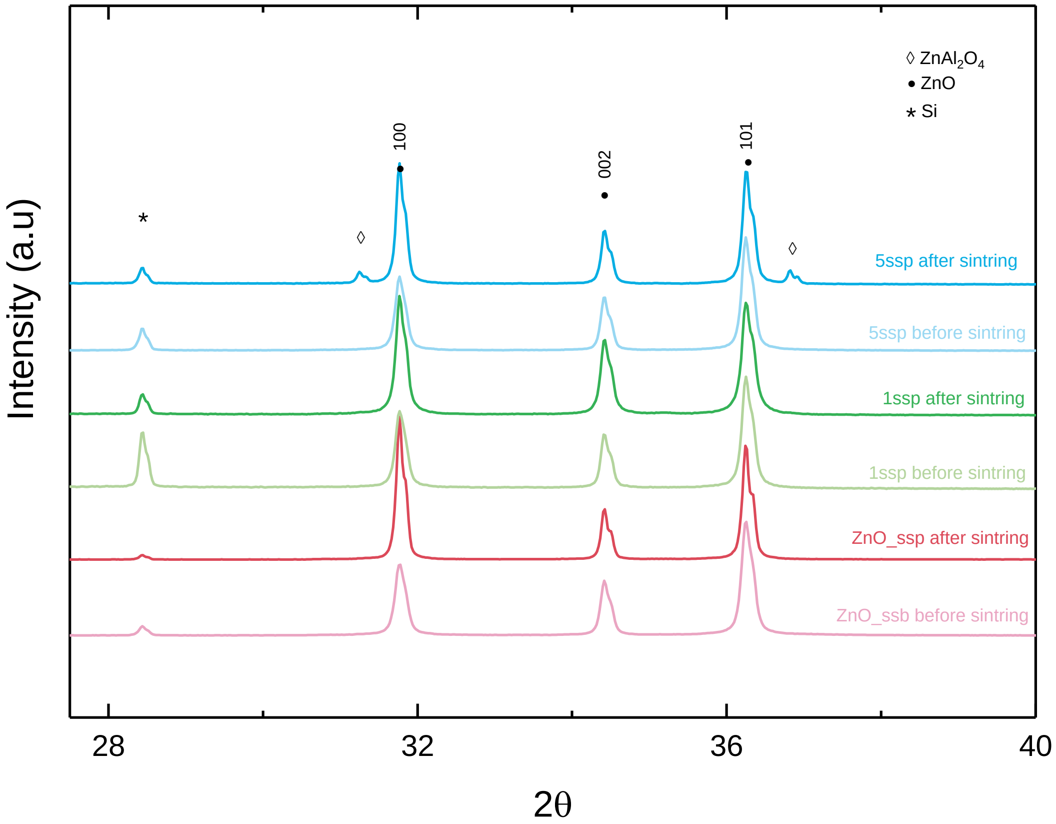

Figure 4.9: : Powder XRD diffractograms from all the samples (0, 1 and 5 mol % Al) prepared by solid state synthesis with planetary ball milling before (brighter pattern) and after sintering (darker pattern) showing strong diffraction peaks from ZnO in addition to weaker peaks from $ZnAl_2O_4$ in the samples with 5 mol % Al. '*' represents preaks from the added Si standard.

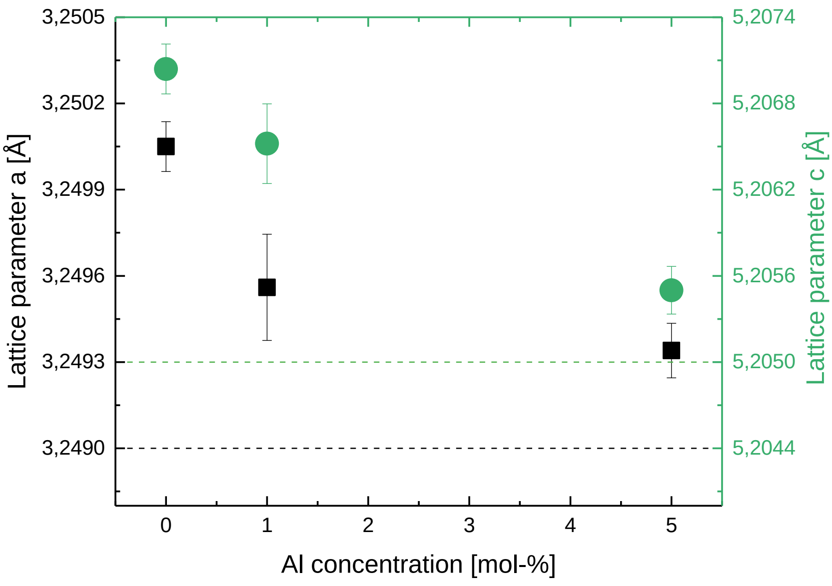

Figure 4.10: Lattice parameters 'a' and 'c' of ZnO determined by powder XRD as a function of Al concentration (mol-%). Black and green symbols correspond to the lattice parameter 'a' and 'c', respectively. Dashed lines indicate lattice parameters from PDF 010708070.

4.2.3 Investigation of microstructure by SEM

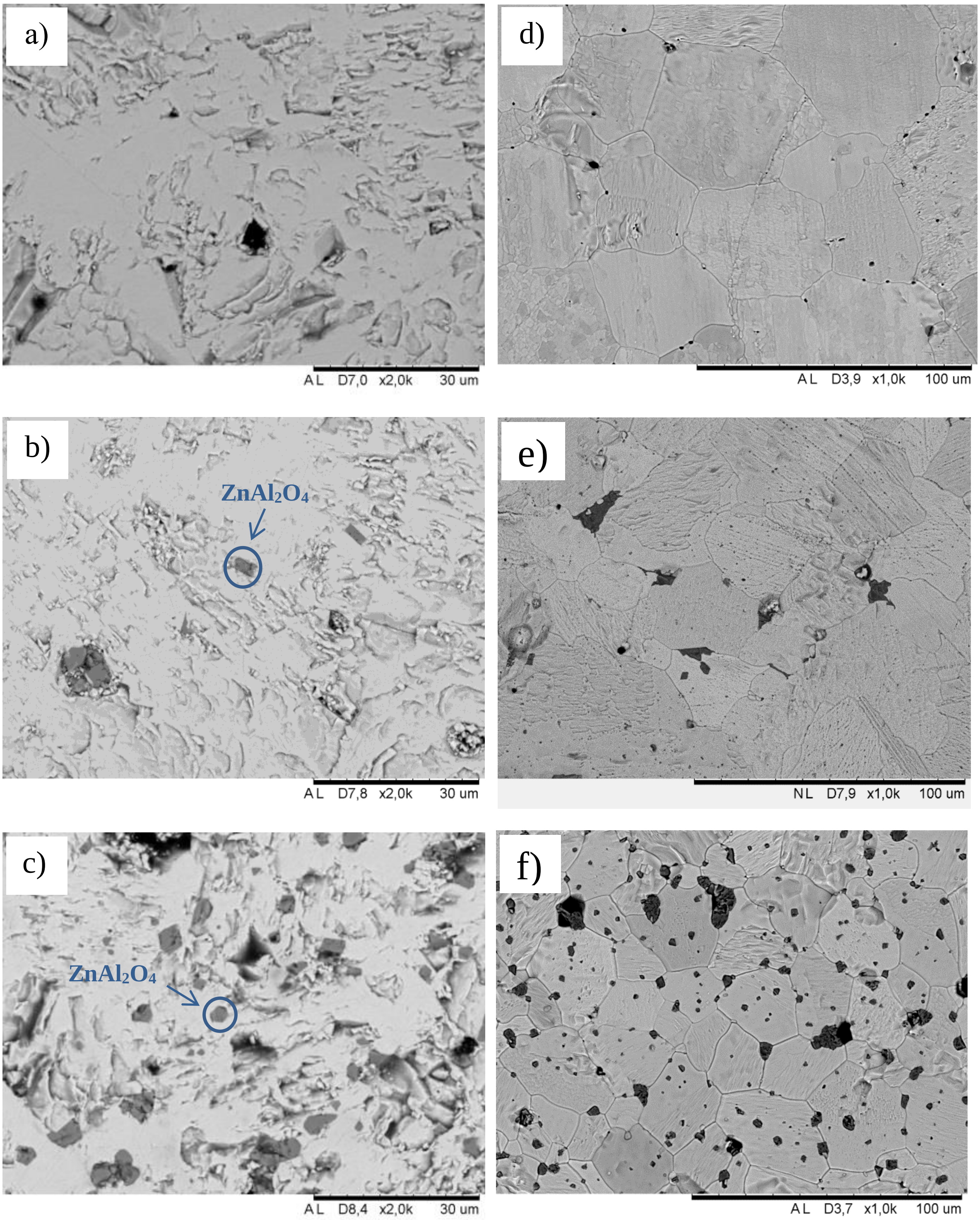

Figure 4.11: Cross-section SEM images of polished (a-c) and thermally etched (d-f) surfaces of ZnO (a) and (d), 1ssp (b) and (e), and 5ssp (c) and (f). They show a clear increase of $ZnAl_2O_4$ particles with Al-content and a corresponding decrease in ZnO grain size.

SEM micrographs of the cross-section for all ssp samples are shown in Figure 4.11 a)-c). Consistent with the XRD results the reference sample shown in a) appears to be single phase ZnO. The darker areas seen are due to pores. For the Al doped samples, the EDX analysis of the darker gray areas confirmed the presence of $ZnAl_2O_4$ as a secondary phase. In contrast to what was evident from the XRD data, $ZnAl_2O_4$, is found in both the 1 mol% and the 5 mol% samples.

As individual grains were not seen on the polished specimens all samples were thermally etched to investigate the influence of ball milling and Al content on the grain size and $ZnAl_2O_4$ location. SEM micrographs obtained with the same magnification for ZnO_ssp, 1ssp and 5ssp are presented in Figure 4.11 d)-f) respectively. Particles of $ZnAl_2O_4$ were mostly detected at the triple points and grain boundaries, while smaller particles dominates inside the ZnO grains. Estimation by eye gives ZnO grain size of ~50, ~40 and ~30µm for ZnO-ssp, 1ssp and 5ssp, respectively. This indicates a decrease of grain size with increasing Al content.

4.2.4 Investigation by STEM EDS

High spatial investigation in TEM was done to detect $ZnAl_2O_4$ nano precipitates in ZnO matrix, but was not detected. Further investigation was done in STEM EDS with the purpose to determine if there were higher concentration of Al at the grain boundaries than in the ZnO matrix. By results from several places and as reported in Figure 4.12, there was not significantly more Al at the grain boundary than bulk. A similar investigation was performed close to grains of $ZnAl_2O_4$ particles, and also there were no higher concentrations of Al detected. However, investigation at grain boundaries between ZnO and $ZnAl_2O_4$ showed Si close to the $ZnAl_2O_4$ grain as shown in Figure 4.13.

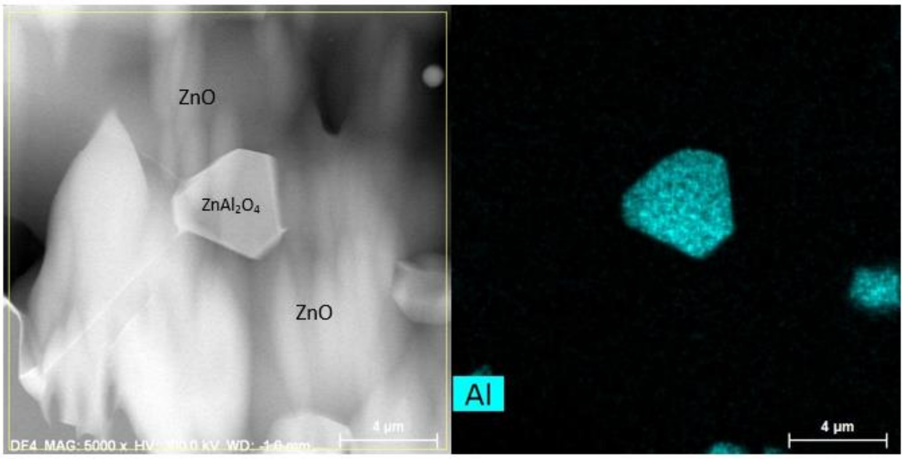

Figure 4.12: STEM EDS on grain boundary between ZnO grains, and between ZnO and $ZnAl_2O_4$ grains to investigate Al content.

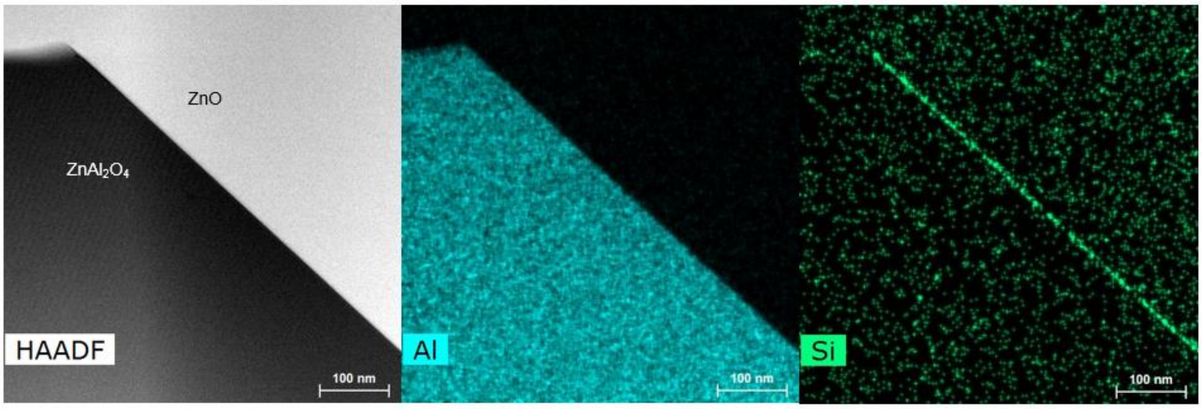

Figure 4.13: STEM EDS done on grain boundary between ZnO grains and between ZnO and $ZnAl_2O_4$ grains to investigate Al content. (b) Si was detected at the grain boundary between ZnO and $ZnAl_2O_4$.

4.2.5 Influence of sintering temperature

The effect of sintering temperature on the electrical properties was investigated by sintering three samples from the same batch, 1ssp. Samples were sintered at 1200^{c}C, 1350^{o}C and 1500^{o}C under the same sintering conditions. Influence of the sintering temperature on electrical conductivity (square) and Seebeck coefficient (circle) are presented in Figure 4.14. As can be seen, the electrical conductivity increases with the sintering temperature. This consistent with the increase in charge carrier concentration as seen from the Seebeck measurements or due to a better grain connectivity.

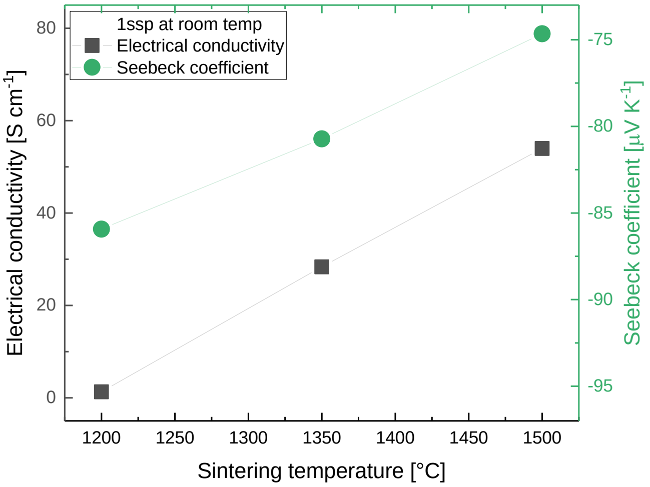

Figure 4.14: Influence of sintering temperature on electrical conductivity and Seebeck coefficient at room temperature for 1ssp

4.2.6 Electrical conductivity measurements

Electrical conductivity as a function of temperature was measured for ZnO_ssp (circle), 1ssp (square) and 5ssp (triangle) as shown to in Figure 4.15a. ZnO_ssp and 5ssp were measured in air without gas flow, while 1ssp in O_2 with continuous gas flow. ZnO_ssp has the lowest electrical conductivity in the range of 19-25 S cm^{-1}, where 5ssp has higher variation in σ and varies from 40 S cm^{-1} to 55 S cm^{-1}. The conductivity decreases up to 500°C and then increases with increasing temperature. 1ssp shows relatively temperature independent conductivity up to 500°C and then increases steeply, reaching values of 100 S cm^{-1}.

The pO_2-dependency of the electrical conductivity for ZnO_ssp (circle), 1ssp (square) and 5ssp (triangle) is shown in Figure 4.15b. The doped samples (1ssp and 5ssp) show only a very small change in σ with different atmospheres. Due to the negligible pO_2 dependency, we can assume the temperature dependent electrical measurements done in O_2 for 1ssp not to be much different if done in air. For ZnO_ssp, a difference in conductivity is observed depending on the atmosphere. A pO_2 independent conductivity indicates that all samples have a dominating donor dopant species, in contrast to the behaviour observed for the sol-gel samples.

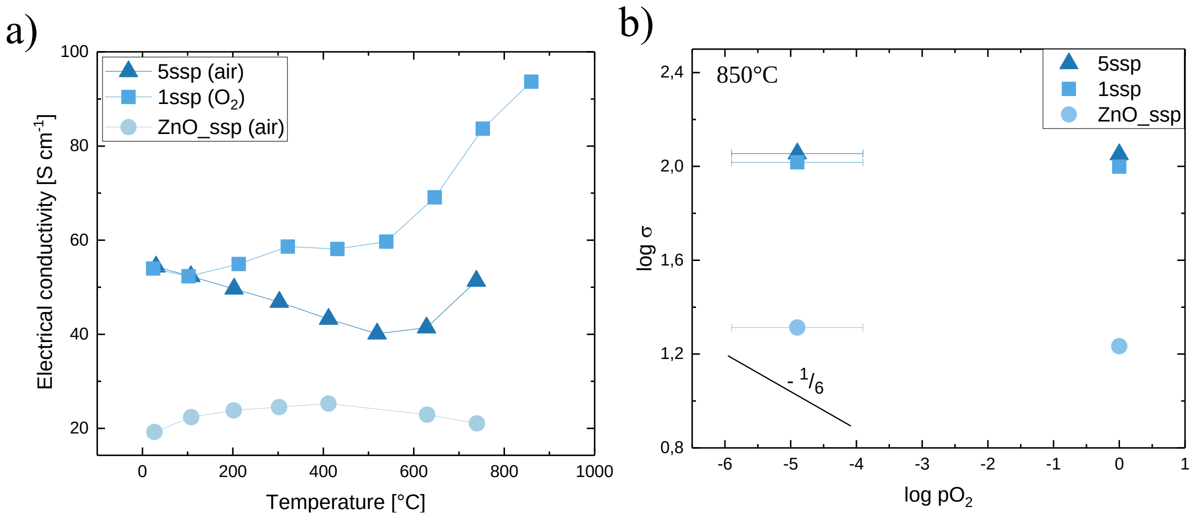

Figure 4.15: a) Electrical conductivity, σ, as a function of temperature for ZnO_ssp (blue), 1ssp (red) and 5ssp (black). b) σ at 850°C as a function of pO_2 for ZnO_ssp (blue), 1ssp (red) and 5ssp (black). Error bars are mostly relevant for measurements in Ar, due to higher sensitivity of leakage.

4.2.7 Seebeck measurements

Simultaneous with the electrical conductivity, also the Seebeck coefficient was measured for 1ssp (square) and 5ssp (triangle), Figure 4.16a. All samples have a large negative Seebeck value indicating an n-type semiconductor. ZnO_ssp has the highest absolute Seebeck coefficient, indicating the lowest charge carrier concentration. 5ssp has the highest charge carrier concentration followed by 1ssp. Samples containing Al have higher charge carrier concentration than ZnO_ssp, which is expected due to doping. The trend for Seebeck corresponds with the electrical conductivity.

The pO_2-dependecy of Seebeck coefficient measured for all ssp samples is shown in Figure 4.16 (right). The measurements were done at same conditions as the electrical conductivity measurements in Figure 4.16b. In agreement with the results for σ, we also observe a change of α by changing the atmosphere. The slope for ZnO_ssp is steeper than for σ, due to measurements done at different time, where data for α is collected after longer time in O_2. Data for 1ssp and 5ssp was collected at the same time as for σ.

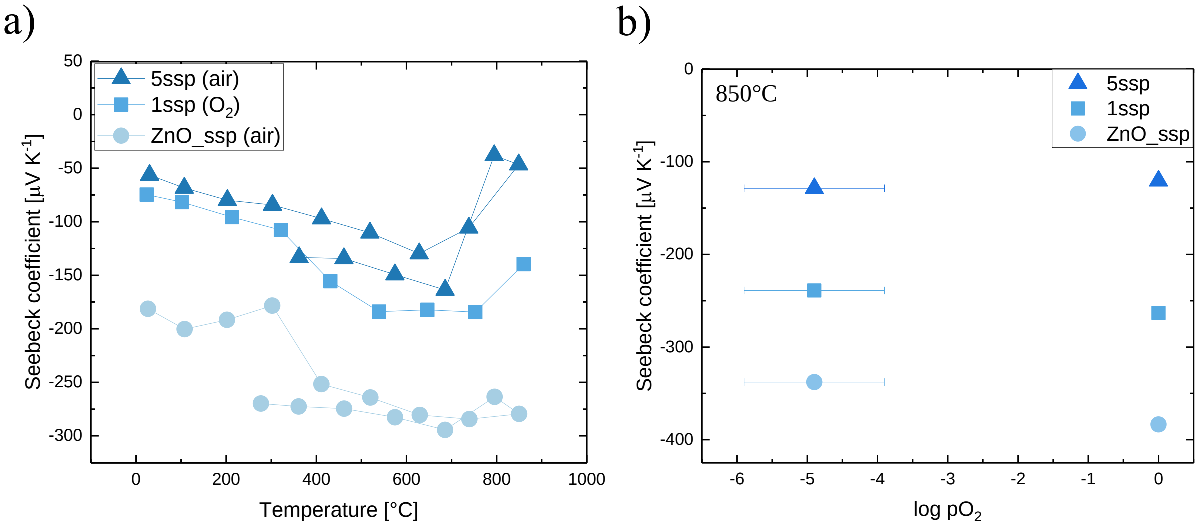

Figure 4.16: a) Seebeck coefficient as a function of temperature for Zno_ssp, 1ssp and 5ssp. b) Seebeck coefficient at 850°C as a function of oxygen partial pressure for Zno_ssp, 1ssp and 5ssp.

4.2.8 Thermal conductivity measurements

The thermal conductivity measured for ZnO_ssp (circle), 1ssp (square) and 5ssp (triangle) as a function of temperature is presented in Figure 4.17a. Measurements were done from 50°C to 800°C with an interval of 100°C. The thermal conductivity decreases with increasing temperature and is the same at high temperatures for all samples. There is more difference between the samples at lower temperature; 1ssp has the lowest conductivity followed by 5ssp and ZnO_ssp with the highest. The measured value differs from 25.1 W m^{-1} K^{-1} to 33.2 W m^{-1} K^{-1} at 50°C. The doped samples follow the same path during cooling, while ZnO_ssp has a small difference. 5ssp has the lowest density of the three samples and in addition smallest grain size. Taking this into account 5ssp would be excepted to have the lowest conductivity, but is not in agreement with the results. There is no obvious reason for this behaviour.

The electronic contribution to the thermal conductivity was calculated from Wiedemann Franz law, presented in equation 18, with interpolated values of the electrical conductivity as an input. The total thermal conductivity and the electrical contribution are presented in Figure 4.17b. The electrical contribution is 0.002% at 100°C and 0.03% at 700°C of the total conductivity. The electrical contribution is therefore neglected in further discussion and the lattice contribution is assumed to be the same as κ_{Tot}.

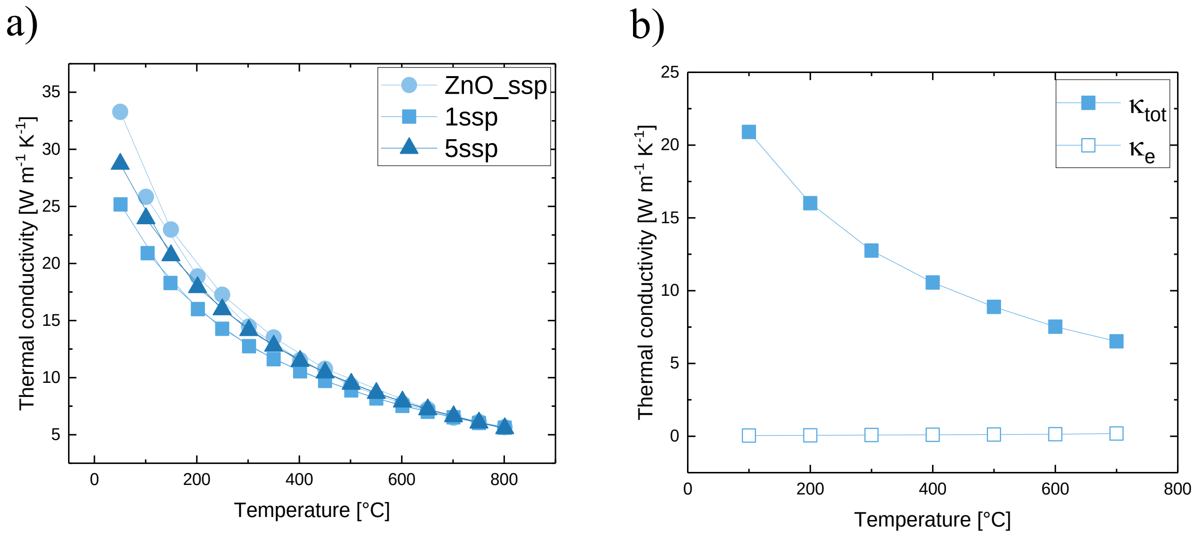

Figure 4.17: (a) Thermal conductivity as a function of temperature for ZnO_ssp, 1ssp and 5ssp. (b) Estimation of the electronic contribution to the thermal conductivity.

4.3 Solid state synthesis by roll ball milling

4.3.1 Colour and density

Figure 4.18: Samples prepared by solid state synthesis with roll ball milling, ZnO_ssr (left), 1ssr (middle) and 5ssr (right), are shown to illustrate the colour difference.

As for the ssp series, also the samples prepared by solid state synthesis with roll milling showed different colour depending on the Al content, Fig. 4.18. However, the colour for samples with the same nominal Al content is different for the different synthesis methods. The colour of the samples varies from Green for undoped ZnO to grey 1ssb and blue-green for 5ssb. The reason for the colour difference is unclear, but it could be due to unintentional impurities.

An overview of the gravimetric density measured for all ssr is given in Table 4.4. All samples has a relative density > 90%, and higher than ≥ 96% for all doped samples, which is higher than for the other synthesis methods.

Sample	Gravimetric density [g/cm^3]	Relative density
ZnO_ssb	5.25	93%
1ssb el	5.55	99%
1ssb term	5.44	97%
5ssb el	5.39	96%

Table 4.4: Gravimetric and relative density measured for samples prepared by ssr.

4.3.2 Phase analysis by powder XRD

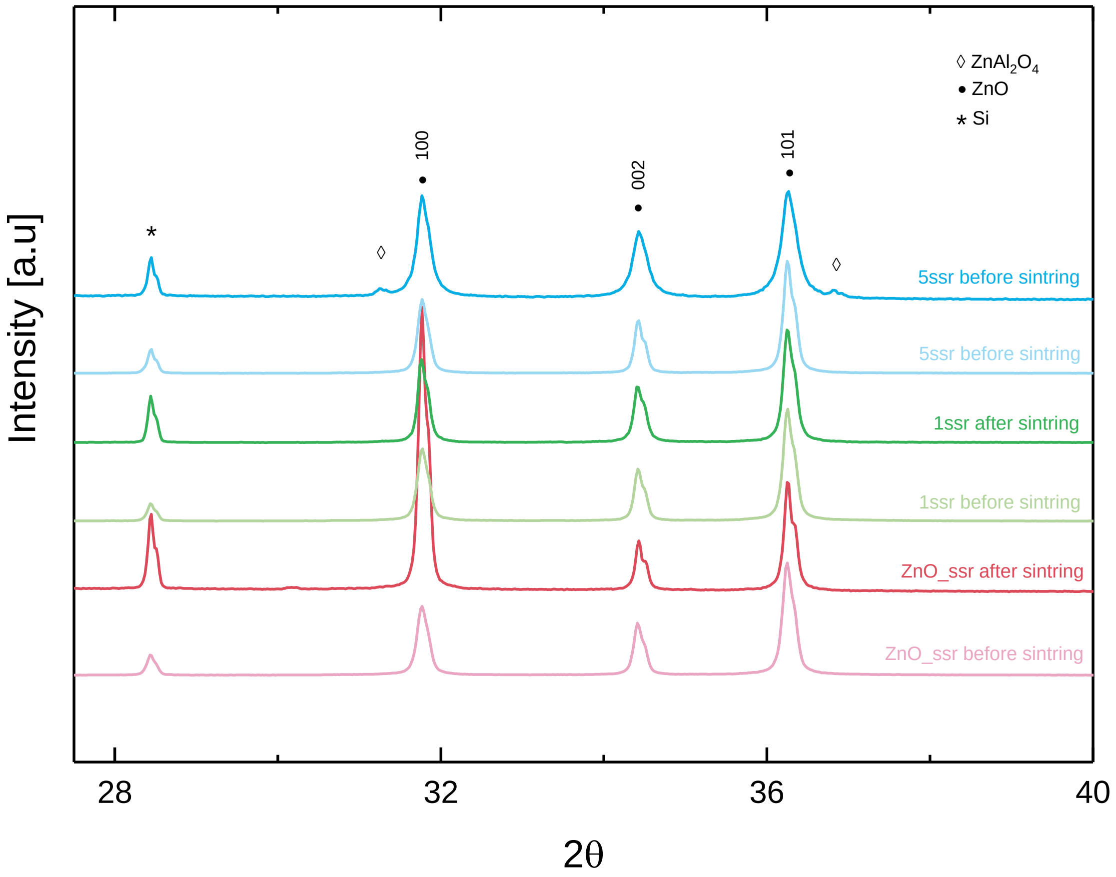

Figure 4.19: Powder XRD diffractograms from all the samples (0, 1 and 5 mol % Al) prepared by solid state synthesis with roll ball milling before (brighter pattern) and after sintering (darker pattern) showing strong diffraction peaks from ZnO in addition to weaker peaks from $ZnAl_2O_4$ in the samples with 5 mol % Al. '*' represents peaks from the added Si standard.

XRD diffractograms of samples prepared by solid state synthesis with roll ball milling are presented in Figure 4.19. ZnO_ssr after sintering has an additional peak at 35°. By comparing the after sintering samples, an increase in reflection width with increasing amount of Al is observed, which may indicate a decrease in particle size. For pure ZnO we observe a decrease in peak width after sintering, which could be due to grain growth.

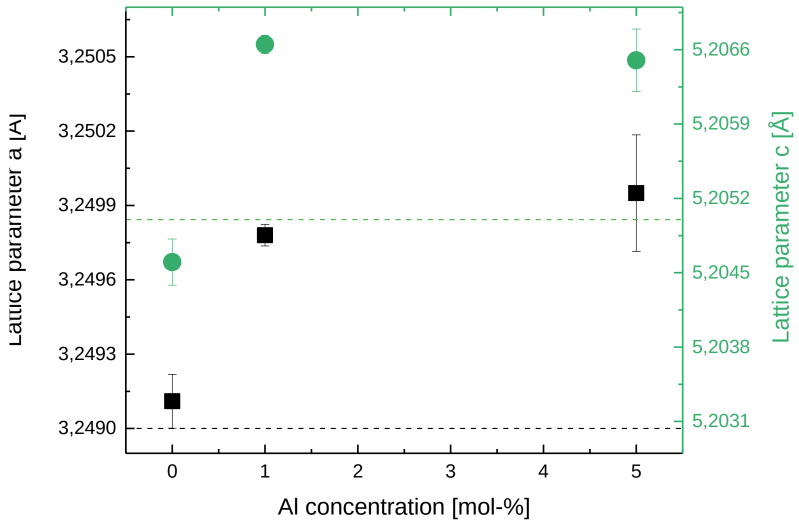

Figure 4.20: Lattice parameter a and c are shown as a function of Al concentration for sintered samples. Dashed lines indicate lattice parameters from PDF 010708070.

The lattice parameters of the different samples, as obtained from the XRD refinement, are shown in Figure 4.20. With increasing Al content, both *a* and *c* increase. However, the ionic radius of Al^{3+} is smaller than that of Zn^{2+}, and one would thus expect rather a decrease in lattice parameters, when increasing the Al concentration within the structure. A possible explanation for the observed, opposite behaviour could include the incorporation of Al at interstitial positions or structural strain created during the synthesis. The latter interpretation is supported by a non-systematic variation of the ratio *a/c* for the different Al levels investigated.

4.3.3 Investigation on microstructure by SEM

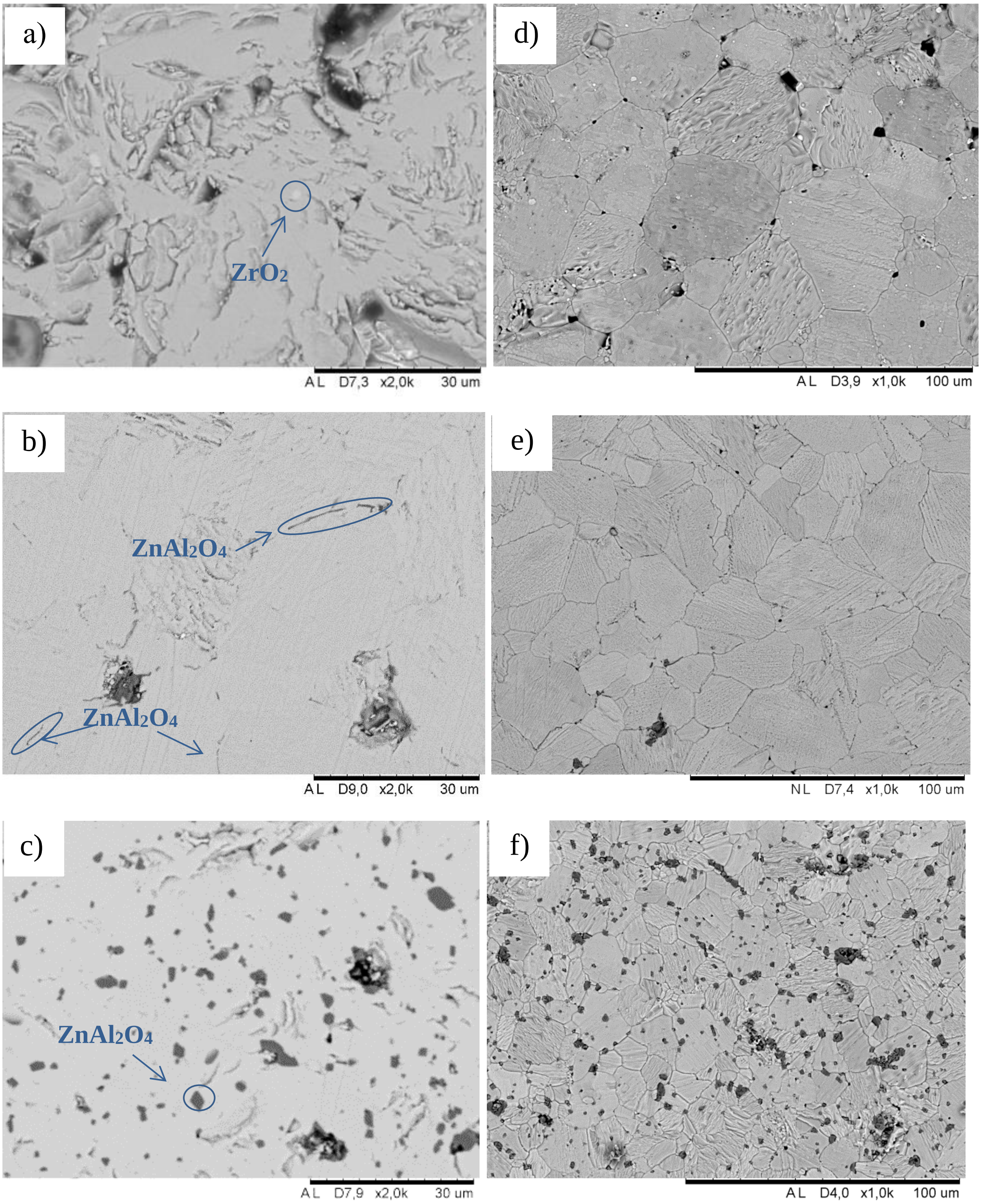

Figure 4.21: SEM images obtained from polished cross-sections with same magnification for a) ZnO_ssr b) 1ssr c) 5ssr and thermally etched with lower magnification for samples d) ZnO_ssr e) 1ssr f) 5ssr.

Investigation of morphology and microstructure of sintered samples was performed by SEM. SEM micrographs obtained of the cross-section of ZnO_ssr, 1ssr and 5ssr are presented in Figure 4.21 a)-c), respectively. Cross-sections were polished for all samples and the images were recorded with the same magnification to enable direct comparison. Consistent with the XRD results, the nominally undoped sample shown in a) is dominated by a primary ZnO phase with a small Zr containing particles (lighter areas), determined by EDX. The darker areas are due to pores and carbon contamination from polishing. For the Al-doped samples the darker grey area correspond to the $ZnAl_2O_4$ spinel secondary phase, as determined by EDX. In contrast to the XRD results, $ZnAl_2O_4$ is clearly found in both the 1 mol% and 5 mol% sample, illustrating the higher sensitivity of SEM as compared to XRD. For 1ssr the shape of the $ZnAl_2O_4$ particles are more thin layers, while 5ssr had more similar particle dimensions.

To further investigate the influence of ball milling and Al content on the microstructure, all samples were thermally etched, Figure 4.19 d)-f). An estimation by eye gives ZnO grain size of ~40µm, ~30µm and ~20µm for ZnO_ssr, 1ssr and 5ssr, respectively. In correspondence with the measured density, ZnO_ssr indeed appears to be the most porous one. Particles of $ZnAl_2O_4$ are found at grain boundaries for 1ssr and randomly distributed for 5ssr (inside grains, grain boundaries and triple joints). Some areas with higher concentration of $ZnAl_2O_4$ are detected. In agreement with the XRD results, a decreasing grain size with increasing Al content is indeed observed in the SEM pictures.

4.3.4 Electrical conductivity measurements

Electrical measurements as a function of temperature for 1ssr and 5ssr are presented in Figure 4.22, with arrows indicating measurement start. The electrical conductivity decreases with increasing temperature for 1ssr, indicating a metallic behaviour, while 5ssr has a small increase. The difference in σ at room temperature is 230 S cm^{-1}, despite this both samples show higher conductivity values during cooling. For 1ssr, this increase is as much as 50 Sm cm-1 at lower temperatures, whereas for 5ssr it is barely visible. The reason for this behaviour is unclear and possible scenarios will be discussed in section 5.2

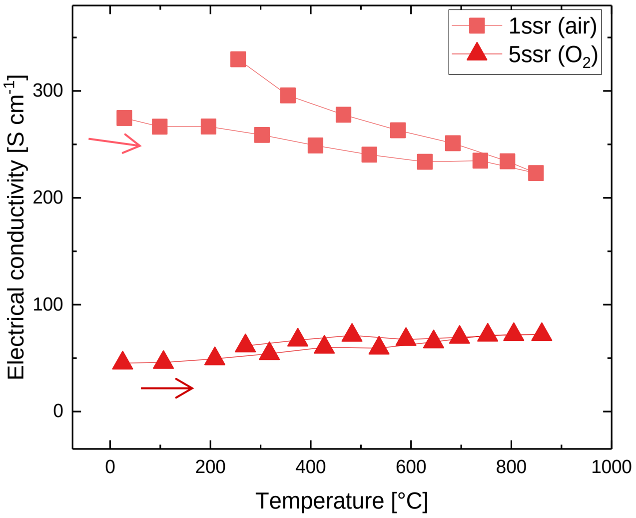

Figure 4.22: Electrical conductivity as a function of temperature for 1ssr and 5ssr.

4.3.5 Seebeck conductivity measurements

Simultaneous with the electrical conductivity, also the Seebeck coefficient was measured for 1ssr, Figure 4.23. The Seebeck coefficient is negative indicating n-type conduction. The absolute Seebeck coefficient is higher during cooling, indicating lower charge carrier concentration. In particular, this implies that the observed increase in electrical conductivity, Figure 4.22, cannot be rationalized by an increase in carrier concentration during the measurement.

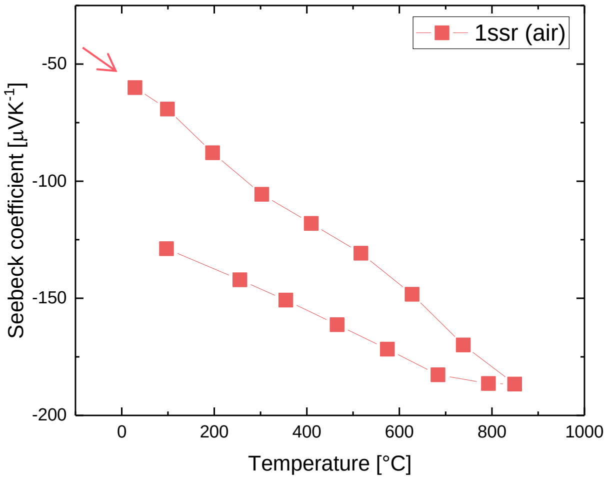

Figure 4.23: Seebeck coefficient as a function of temperature for 1ssr.

4.3.6 Thermal conductivity measurements

The thermal conductivity as a function of temperature for 1ssr is shown in Figure 4.24. The thermal conductivity decreases with increasing temperature and follows the same trend while cooling. The electrical contribution to the thermal conductivity is calculated from Wiedemann Franz law, (eq 16). The contribution at 100oC and 800oC is 0.24 W m-1 K-1 and 0.59 W m-1 K-1, respectively which makes 0.01% and 0.1% of the total thermal conductivity.

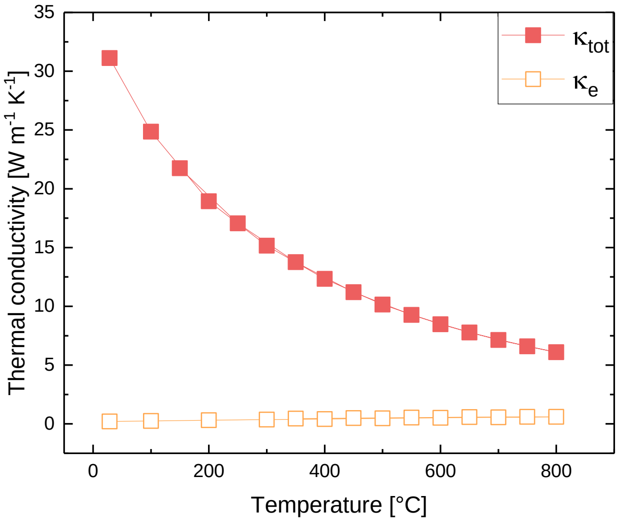

Figure 4.24: Thermal conductivity of 1ssr as a function of temperature.

4.3.7 Reproducibility

In comparison to all other samples synthesised here, 1ssr shows very different values of sigma and Seebeck coefficient, and different behaviour during thermal cycling. Therefore, this particular composition was investigated further, by synthesis of a new sample (1ssr_b2) and remeasuring the properties.

Density

The density of the different 1ssr samples is presented in Table 4.5. 1ssr_b2 is from a new batch with the same composition and sintering conditions as 1ssr, but shows a slightly lower density than the previously prepared samples.

Sample	Archimedes density [g/cm^3]	Relative density
1ssr el	5.55	99%
1ssr term	5.44	97%
1ssr_b2	5.34	95%

Table 4.5: Density of different 1ssr samples.

Electrical conductivity measurements

Figure 4.25a shows the electrical conductivity of one sample, 1ssr, were the suffix *r_1* indicates the measurement cycle. The sample was polished between each measurement to exclude any surface changes during measurement. The sample shows an increase in conductivity for each run. Note that the electrical contact broke during both second and third measurement, but it seems that the last measurement of one cycle corresponds to the first measurement of the next cycle, indicating that neither the placement of the van-der-Pauw contacts, nor the removal of the surface layer have a significant influence on the results.

The results of an equivalent thermal cycling experiment on the second sample, 1ssr_b2, are shown in Figure 4.25b. Also this sample shows a qualitatively similar, unconventional behaviour, with conductivity values somewhat lower. The latter can most likely be related to the lower relative density of 1ssr_b2 compared to 1ssr.

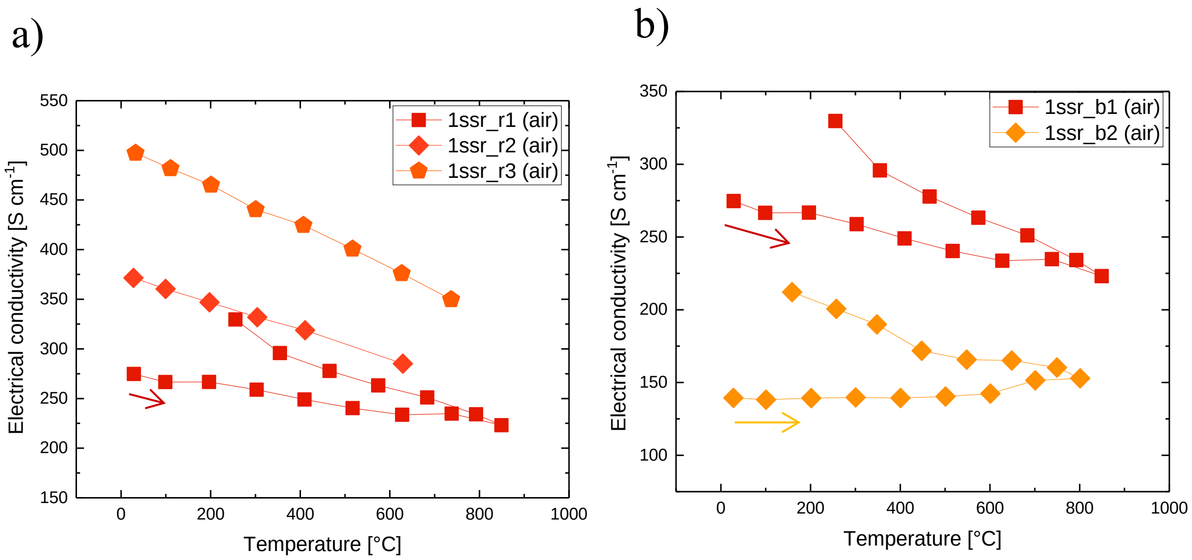

Figure 4.25: a) Electrical conductivity as a function of temperature remeasured for 1ssr. b) Electrical conductivity as a function of temperature of 1ssr_b1 and 1ssr_b2.

Seebeck measurements

The Seebeck coefficient for 1ssr was measured during three thermal cycles, Figure 4.26. The result for 1ssr, Figure 4.23 is qualitatively confirmed. Interestingly, the results from the last measurement of each cycle are different from the first measurement of the next cycle. This could be related to a change of thermal contact between thermocouple and sample during the measurement.

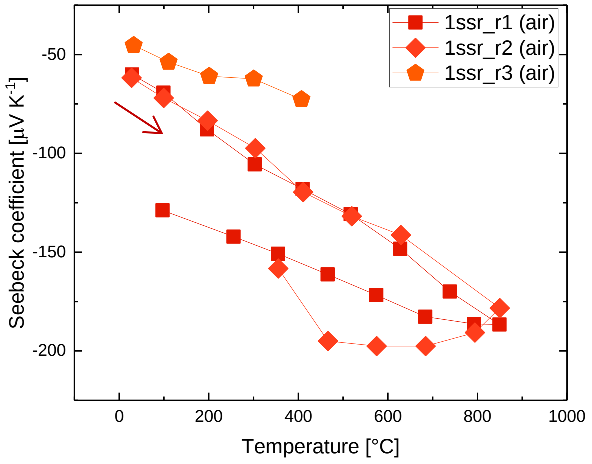

Figure 4.26: Seebeck coefficient as a function of temperature remeasured for 1ssr.

Chapter 5

Discussion

In this chapter, the results presented in the previous chapter will be discussed. The discussion will be divided into two parts, whereas the microstructure will be discussed first, followed by the thermoelectric properties.

5.1 Influence of synthesis method and composition on the microstructure

Influence of ball milling technique on microstructure

Comparing the ZnO samples prepared by the two solid-state synthesis techniques, planetary and roll ball milling, no significant difference is observed. However, comparison with ZnO synthesised without ball milling (Appendix B) a decrease of the ZnO grains is observed by ball milling. Even though the ZnO grains seems to be similar a more subtle difference between the samples is the difference in precipitate size: While $ZnAl_2O_4$ precipitates in samples mixed and crushed by planetary ball milling are rather large; the respective grains are much smaller in samples using the roll milling technique. This observation is at first surprising, as the kinetic energy of balls within the planetary ball mill is much higher, and one would thus expect finer grains in the resulting product, as compared to the roll milled samples.

This could be due to higher energy introduced to the system by planetary milling creating smaller grains with higher surface energy, forming an intermediate phase during the milling process. This have been reported for other binary oxides [41]. However, no reflections corresponding to $ZnAl_2O_4$ were detected in XRD after milling. XRD of the ZnO and Al_2O_3 powders (before ball milling) indicates broader peaks for Al_2O_3 than ZnO (Appendix E). There could be several reasons for this, such as smaller particles, more structural defects or a more amorphous precursor material. However, this makes Al_2O_3 more difficult to detect both before and after milling. A hypothesized smaller particle size of the planetary powder as compared to the roll milled one would also decrease the reaction temperature and therefore increase the available time for grain growth during sintering. However, no clear conclusion on the particle size distribution after milling can be drawn from XRD to support or disprove this scenario. There is also need for investigation of the influence of number of ball for the two techniques in order to compare them with different parameters. Further TEM studies of the powder before and after milling could help determine the influence of Al during ball milling.

The grain growth mechanism for the ZnO and Al_2O_3 may be behind the puzzling presence of secondary phase $ZnAl_2O_4$ for 1% Al. Han *et al.* [42] have explained their similar observations for solid-state samples with a microscopic model reproduced in Figure 5.1. In their model, the spinel phase acts as a type of electrolyte, transporting both Zn and Al ions. While Al diffuses from the unreacted Al_2O_3 through $ZnAl_2O_4$ to be then dissolved within ZnO as a dopant, Zn is transported towards the $ZnAl_2O_4$-Al_2O_3 interface forming more of the spinel phase. By this process, a simultaneous increase of Al concentration within the ZnO matrix and the formation and growth of $ZnAl_2O_4$ can be rationalized.

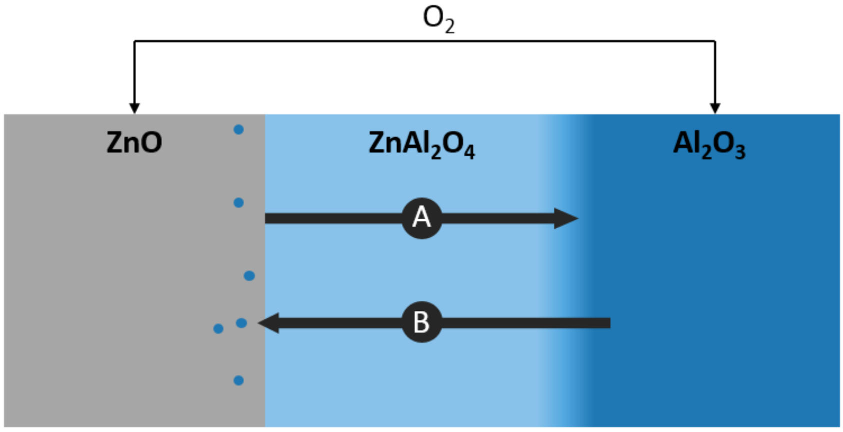

$$A:\quad Zn^{2+} + 2e' + \frac{1}{2}O_2 + Al_2O_3 \rightarrow ZnAl_2O_4$$

$$B:\quad Al_{Al}^{x} + \frac{1}{2}O_2 \overset{ZnO}{\rightarrow} Al_{Zn}^{\bullet} + O_O^{x} + e'$$

Figure 5.1: Schematic diagram for the solid-state reaction process of ZnO and Al_2O_3, modified from [42.]

Influence of Al on microstructure

For all samples prepared by the two solid-state synthesis techniques, a decreasing grain size of the ZnO phase was observed, when the Al content increased. This general trend is in agreement with previous reports in the literature [43-47].

A possible scenario for the decreasing average grain size with Al content is the presence of $ZnAl_2O_4$. Indeed, $ZnAl_2O_4$ precipitations are mostly found on the triple joint between different ZnO grains. $ZnAl_2O_4$ thus seems to act as a pinning centre, preventing grain growth of the ZnO matrix [8, 43]. The possible influence of the reduced grain size on the thermoelectric properties will be discussed in the next section.

White layer on specimen after sintering

After sintering, a thin white layer was found on the solid-state samples and the walls of the crucible (Appendix C). This has also been reported by Bérardan *et al.* [43]. The thickness of the layer seemingly increased with increasing Al concentration in the samples and was not detected for the pure ZnO samples. EDX and XRD analysis of the powder identified it as $ZnAl_2O_4$. Segregation of $ZnAl_2O_4$ from grain boundaries to the pellet surface or of Al from the alumina crucible to the sample could also cause presence of more $ZnAl_2$O4 at the surface. However $ZnAl_2$O4 would then have been detected at the pure ZnO samples, in addition was sacrificial powder used to prevent direct contact between the crucible and sample. An EDX analysis on the fractured sample cross section did not show a trend of increasing Al concentration towards the surface. Since the white layer was also found on the crucible walls, evaporation of ZnO/Zn from the sample and reaction to $ZnAl_2O_4$ with the crucible wall is thus a likely scenario. The sample surface will then appear enriched with the remaining $ZnAl_2O_4$.

5.2 Influence of synthesis method and composition on thermoelectric properties

Undoped sol-gel samples

Based on electrical and Seebeck measurements, Figure 5.2, sol-gel samples show a much lower electrical conductivity than the other Al containing samples and a Seebeck coefficient in the same range as the undoped ZnO sample. Further, the pO_2-dependency of the electrical conductivity and Seebeck coefficient correspond to oxygen vacancies as the dominating defect, not the targeted Al-acceptors, as for the solid-state samples. These observations clearly indicate that only a negligible fraction of Al was solved in the structure for the sol-gel samples.

Unlike for the solid state synthesis technique, where precursors are crystalline substances, with slow reaction kinetics driven by cation diffusion, the gel contains the metal atoms incorporated within an organic complex, i.e. not in a crystalline state. The resulting phase composition is thus dependent on the combustion temperature of the complex and the chemical driving force for the reaction of the specific compound. It is plausible to assume the formation of $ZnAl_2O_4$ from the combusted gel to occur at lower temperatures than the crystallization of ZnO, i.e. that all Al-species are already consumed in the formation of $ZnAl_2O_4$, and that the crystalline ZnO formed at higher temperatures will thus be effectively undoped. Different temperatures have been reported for the formation of $ZnAl_2O_4$, 400°C [48] and 600/620°C [49], while for ZnO 520 °C [50]. We calcinated at 500ºC and XRD taken of the powder of ZnO with 1% Al after the first calcination didn't reveal any peaks for $ZnAl_2O_4$, (Appendix D) however as mentioned earlier due to the detection limit of the technique. Therefor a further investigation by for example *in situ* XRD or calorimetric methods of ZnO with higher Al content may be interesting and helpful to clarify this unusual behaviour.

Electrical conductivity and Seebeck coefficient

Al-substitution is known to be an effective dopant to enhance the mobile electron concentration of ZnO. However, also microstructural factors, such as pores, precipitates and defects affect the electrical conductivity. The Seebeck coefficient on the other hand is less dependent on microstructure or presence of precipitates, but highly sensitive to the charge carrier concentration. In Figure 5.2, a summary of the electrical conductivity (a) and the Seebeck coefficient (b) measured at room temperature for all samples is shown. As discussed in the previous section, sol-gel synthesised samples show very low conductivity combined with values of the Seebeck coefficient resembling virtually undoped samples. For the other synthesis methods, no clear trend with the nominal Al concentration could be observed, despite the initial increase of electrical conductivity from 20 to 50 S cm^{-1} and Seebeck coefficient from -180 to -75 μVK^{-1} upon introduction of 1 mol% Al for planetary milled samples.

The 1% roll milled sample stands out, showing significantly higher conductivity than the other doped samples, despite the very similar Seebeck coefficient, and possible reasons for this behaviour will be discussed in the following.

The presence of $ZnAl_2O_4$ phase could affect the electrical conductivity, since it is reported as an isolator [10], which could cause lower conductivity for 5% Al samples as compared to 1%. However, it does not explain the observed difference between the 1% samples. If the precursor powders weren’t mixed homogeneously, it could lead to a higher content of Al in some samples from the batch, on expense of other samples with a lower content. To investigate this further, different samples from the same batch were measured showing effectively the same conductivity. The amount of the secondary phase was similar for those samples and STEM-EDS did not reveal any peculiarly high content of Al at the grain boundary. However, the shape of the $ZnAl_2O_4$ particle was more like a thin layer decorating the ZnO grains. This should contrary lower the electrical conductivity, because the secondary phase in an isolator.

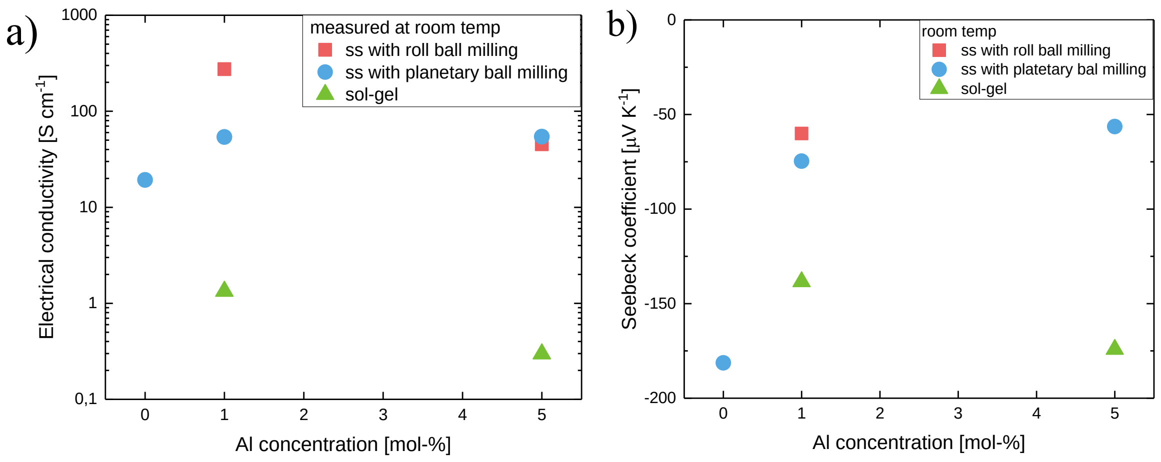

Figure 5.2: Values of the electrical conductivity (a) and Seebeck coefficient (b) at room temperature.

To ensure that the positioning of the electrical contacts or other experimental artefacts was not the problem, the measurement was repeated several times on the same sample with intermediate grinding of the surface layer. During each cycle, the electrical conductivity continued to increase, Figure 4.25 and was not observed for planetry milled samples (Appendix F). This indicates that the measured values are not an experimental artefact, nor a property of a possible, highly conductive surface layer, but rather reflect the properties of the bulk.

Another hypothesis was to explain the high conductivity by an additional, unintended doping species, introduced into this particular batch of powder during synthesis. In order to investigate this scenario, a new batch of the same composition was made under the same conditions (1ssr_b2). Electrical measurements showed slightly lower conductivity values, but still significantly higher than the other samples. In addition, the 1ssr_b2 sample also showed the unexpected continuous increase in conductivity during thermal cycling.

Our 1% roll milled samples has in fact the highest geometrical density of the samples fabricated in this thesis. Micro pores or limited mutual adhesion between grains could act as scattering centres and limit carrier mobility [8]. By comparing the relative density of the samples, the 1% roll milled has the highest relative density with 99% compared to the 1% planetary milled sample with 96%. The sample from the second batch, 1ssr_b2, had a lower relative density, 95%, but still showed a significantly higher conductivity than the planetary sample, indicating that the density difference can in fact explain the difference between 1ssr_b2 and 1ssr, but does not account for the overall spread in experimental results.

Defects in the crystal structure such as stacking faults, twins and dislocations [8] could also affect the electrical conductivity. Further TEM studies are therefore needed to understand these results better. Measurements of the Hall effect would further help to disentangle the complicated interplay of carrier concentration and mobility. In particular, *in situ* measurements would be useful to understand the puzzling behaviour during thermal cycling.

Comparison with literature

It is instructive to compare the results obtained here with values reported for similar compositions in the literature, Figure 5.3. The roll milled sample, which has by far the highest conductivity in our study, shows in fact an electrical conductivity in the same range as literature, while the other samples all show a lower conductivity.

Not only the magnitude, but also the temperature dependency for the sample is different: While the planetary milled samples show an increasing conductivity with increasing temperature, the 1% roll milled sample as well as the literature data show the opposite trend.

However, the Seebeck coefficient of both samples is similar and in good agreement with literature, both for the magnitude *and* the temperature dependence.

For our best, 1% roll milled sample, the thermopower is slightly higher than data reported by Cai *et al*. [11], indicating a lower charge carrier concentration. However, we still obtained a higher electrical conductivity for that sample, i.e. a higher carrier mobility. This can be related to the different geometrical densities: While Cai *et al*. reported a relative density of 95%, and Zhang *et al*.[46] 96% our sample had a relative density of 99%. In contrary with literature, we did not obtain similar density for all our samples, which makes the comparison more difficult. Better control of the density would therefore be necessary for minimizing the influencing factors.

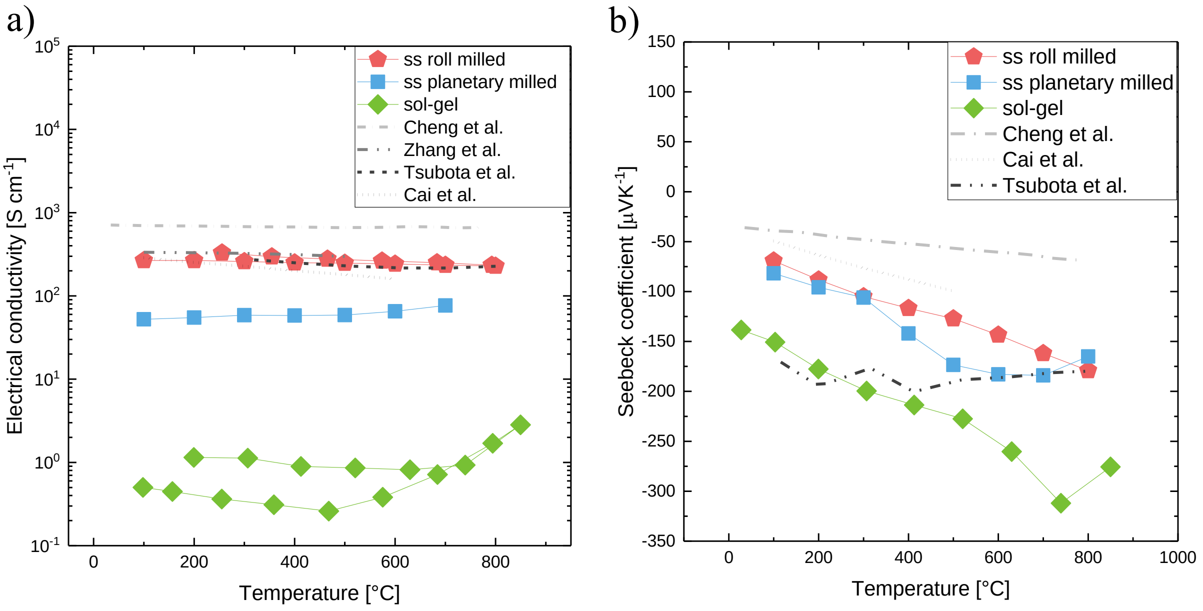

Figure 5.3: Comparison of electrical conductivity (a) and Seebeck coefficient (b) for solid-state samples with 1% added Al with reported values for ZnO with nominal 1% Al [10,11,46,47].

Thermal transport properties

The initial goal of this work was to investigate means to reduce the high lattice thermal conductivity of ZnO via engineering of the microstructure of the investigated samples. The thermal conductivity could be affected by factors such as secondary phase, grain boundaries, pores and lattice defects. In our study, we obtained thermal conductivity of ~30 W m^{-1} K^{-1} for pure ZnO at room temperature, while Tsubota *et al*. [10] reported ~ 50 W m^{-1} K^{-1}. This could indicate planetary ball milling is more suitable for reduction of κ than roll ball milling done by Tsubota *et al.*

From Figure 4.17 it is noted that the thermal conductivity is slightly lower for Al-doped samples than the undoped sample at lower temperatures. This can be rationalized by an increased scattering rate of phonons at the Al point defects. At higher temperatures, however, all compositions show basically identical values for the lattice thermal conductivity.

The influence of synthesis method on the thermal conductivity was investigated by measuring ZnO with 1% Al for all synthesis methods, Figure 5.4. The lattice thermal conductivity was calculated to neglect the electrical contribution - as the contribution differs depending on synthesis methods - and plotted as log (κ_L) as a function of log (T). The observed approximate T-1 dependency indicates dominating Umklapp scattering and is expected above Debye temperature (θ_D ~ 420 K for ZnO [51]).

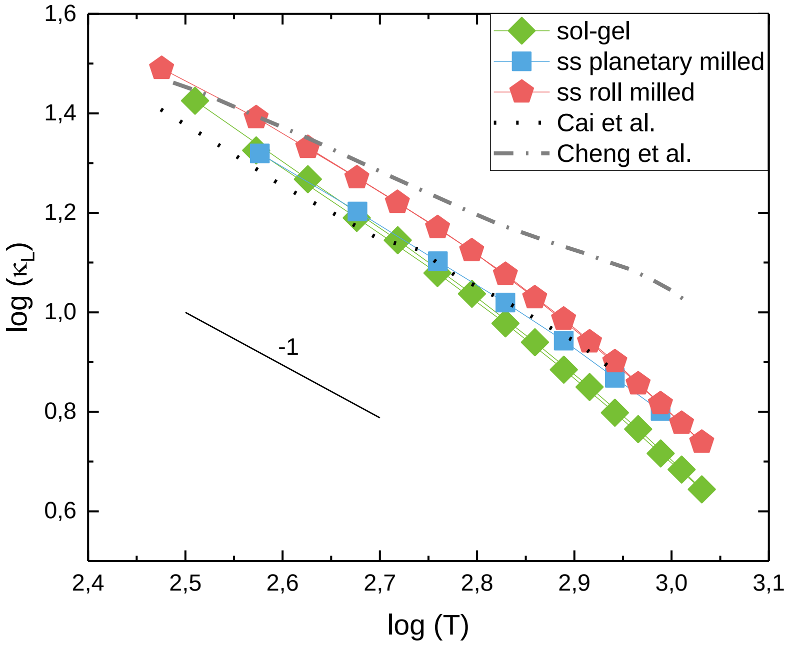

Figure 5.4: Temperature dependency of the thermal conductivity of all ZnO samples with 1% Al, compared with reported values for ZnO with nominal 1% Al content [11,47].

There is still a small difference in the lattice thermal conductivity, with the lowest conductivity observed for the sol-gel sample and highest for roll milled. This difference could be due different densities of the samples. As mentioned earlier does porosity influence the thermal conductivity [44]. The measured density of the sol-gel sample is in fact lowest, while that of rolled milled is highest. However the synthesis methods does not show any large influence on the lattice thermal conductivity. At higher temperature Umklapp is dominating and decreasing the density or grain size will thus not show a large effect. Therefore other approaches such as nano precipitates or complex structures are necessary to decrease the lattice thermal conductivity. To obtain nano-precipitates, an optimization of the calcination and sintering conditions, such as time and temperature is important to prevent growth of large $ZnAl_2O_4$ precipitates, since sol-gel in general needs lower reaction temperatures than solid-state methods [52].

Figure of merit

The figure of merit (zT) is calculated from the electrical conductivity, the thermal conductivity and the Seebeck coefficient. The temperature dependency of zT for ZnO samples with different nominal composition of Al prepared is presented in Figure 5.5a, where the sample with 1% added Al shows the highest zT, while 5% is the lowest. Due to the small increase in conductivity with increasing Al content, contrasted with the significant drop of the Seebeck coefficient, the 5% doped sample shows a lower zT than the pure ZnO.

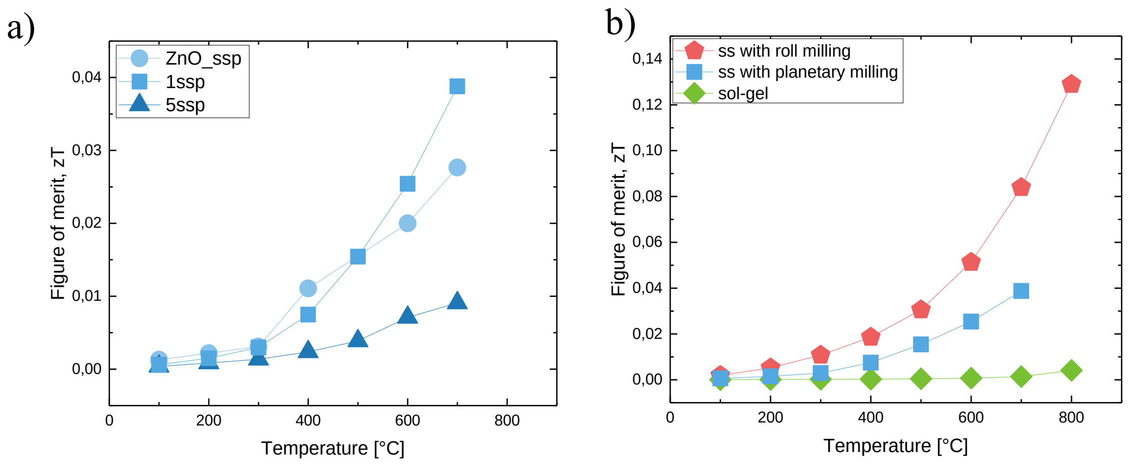

Figure 5.5: zT as a function of temperature for different Al content (a) and different synthesis methods (b).

To compare the influence of synthesis method on zT, ZnO samples with 1% Al content are shown for all synthesis methods in Figure 5.5b. As expected from the low electrical conductivity does the sol-gel sample have the lowest zT. The roll milled sample shows the highest zT - as expected - due to high electrical conductivity, while the thermopower and thermal conductivity is similar to the planetary sample. zT increases with temperature for all samples. The roll milled sample reaches a zT of 0.13 at 800ºC, which is higher than reported by Cheng *et al.* (~0.04 at 800ºC) [47] for the same composition, but lower than Ohtaki *et al.* [10] (~0.2 at 800ºC). However, Ohtaki *et al.* reported higher thermopower than others, which leads to a higher zT. The highest obtained zT for Al doped ZnO is 0.44 at 725°C by Jood *et al.* [12] by lowering the lattice thermal conductivity ($\kappa_{725°C} < 2.0$ Wm^{-1}K^{-1}) via a nano-composite approach with particles of at least 1µm. Also Nam *et al.* [13] reported a high zT of 0.34 at 800°C also due to obtained nano-precipitates of 200nm. While the nano-composite approach may be effective in generating high zT values, more work on the long-term stability of at high temperature and under cycling is needed.

5.3 Further work

From the discussed topics it should be clear that a more fundamental study of electrical behaviour and sol-gel synthesis should be conducted. In the following section, possible further experiments are suggested in order to reach a better understanding of the presented observations.

- Thermogravimetric analysis with Differential Scanning Calorimetry (TGA-DSC) is encouraged for the sol-gel combustion in order to investigate the formation temperature for ZnO and $ZnAl_2O_4$. It will also provide guidance in preventing ZnO evaporation during sintering.

- Influence of sintering temperature, whereas lower temperature could be used for sintering of sol-gel to obtain smaller grain size, especially since $ZnAl_2O_4$ was formed before 900ºC. Considering the impact of mechanical milling of on the sintering temperature, an comparison between the grain size of the two milling techniques at different temperature would be interesting. Shorter heating and sintering times, for example by using an spark plasma sintering (SPS) instrument, are also likely to be beneficial in order to decrease grain growth during sintering.

- Hall effect measurements of the samples, especially the 1% roll milled before and after electrical measurements to investigate if there is a change in the charge mobility. Temperature dependent Hall effect measurements may even provide relevant information *in situ*.

- TEM studies on 1% roll milled and planetary milled to investigate the difference in microstructure by ball milling. In addition to further studies on the grain boundaries of the 1% roll milled sample, by FIB sample preparation close to the thin layer of the secondary phase.

- Investigation on powders before and after milling to determine the effect of ball milling by TEM. Also, more detailed XRD refinement to investigate the influence on the structure.

- Further refinement of parameters during ball milling, for example the number of balls and rotation speed, in order to map out the influence of potential contaminations during milling.

- Variation of the synthesis procedure of the sol-gel method, by changing the amount of complexing agent or pH of the used solution, in order to modify the crystallisation behaviour of the different phases.

- In order to increase the zT values, additional doping with other elements may be a viable route. Promising results on a co-doping approach have recently been reported.

Chapter 6

Conclusions

In this project, the influence of three different synthesis methods on structural and thermoelectric properties of Al-doped ZnO was investigated.

The structural investigation showed $ZnAl_2O_4$ precipitates for all samples with added Al, with smallest particle size for sol-gel and largest for solid state with planetary ball milling. The size of ZnO grains was similar for all samples for nominal 1% Al content. This, in addition to large $ZnAl_2O_4$ precipitates after the second calcination for sol-gel, show that lower sintering temperatures is needed to prevent grain growth and obtain nano-precipitates.

For the solid-state samples a decrease in ZnO grain size with increasing Al content was observed, due to growth inhibition due to a pinning effect by the precipitates. The ball milling techniques did not show any large impact if the ZnO grains, but $ZnAl_2O_4$ particles were found to be smaller for samples prepared by roll ball milling and for the sample with nominal 1mol% Al content a thin layer of the secondary phase decorating the ZnO grains was observed. Larger amount of $ZnAl_2O_4$ at the surface of the sintered samples were observed due to high sintering temperature causing evaporation of Zn/ZnO, while leaving $ZnAl_2O_4$ behind.

Sol-gel samples were found to be effectively undoped, based on their poor electrical conductivity, low Seebeck coefficient and *in situ* measurements of their pO_2-dependency. The latter reveal oxygen vacancies as dominating positive defect for the sol-gel samples, contrary to the samples prepared by the solid state method, where the substituted Al is – as expected – the dominating positive defect. The reason for the sol-gel samples being undoped is unknown, but rationalized to be a result of different formation temperatures for the two components.

For the solid-state samples enhanced electrical conductivity and Seebeck coefficient was observed with increasing sintering temperature. For all samples with added Al the Seebeck coefficient was in the similar range temperature of -70 to -50μVK^{-1} at room temperature, which is comparable with reported values. The electrical conductivity was lower than the majority of the literature for all solid-state samples, with the highest value of ca. 50 S cm^{-1}. A notable exception is the 1% roll milled sample, with an electrical conductivity of almost 300 S cm^{-1} at room temperature. This sample further showed an increase in electrical conductivity upon thermal cycling, contrary to the other samples. This behavior was also observed in an individually synthesized new sample, but has not been reported and the reason is unknown.

There was no clear variation of the thermal conductivity κ with nominal Al content, neither with the chosen synthesis method. At high temperatures, κ was found to be dominated by Umklapp scattering, so that neither point defect scattering by the added Al species, nor grain boundary scattering by the different particle sizes was effective to reduce κ.

Finally, the roll milled sample with 1% nominal Al content showed the highest *zT* of 0.13 at 800°C, with further need of optimizing the synthesis method to enhance the zT.

Appendix A

Phase diagram

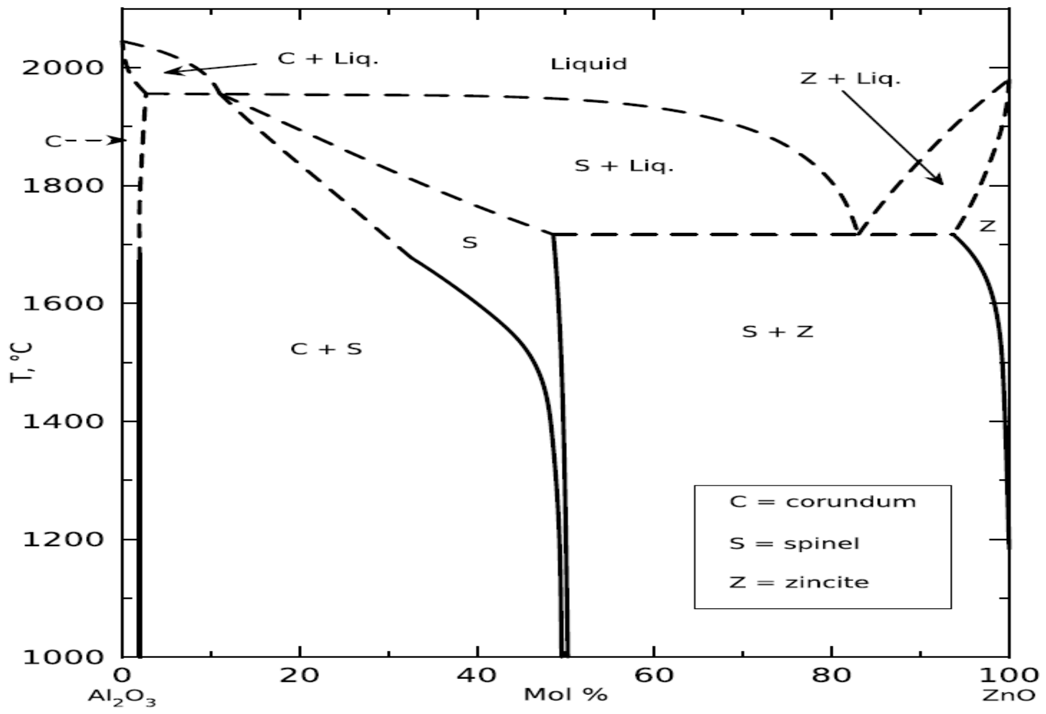

Figure 6.1: Phase diagram of Al_2O_3 and ZnO [53].

Appendix B

Reference sample

A reference sample was prepared by solid-state synthesis without ball milling to compare the influence of ball milling.

Colour of sample

Figure 6.2: An image of ZnO_ss0 was taken to illustrate the colour of ZnO pellet if not exposed to any additional treatment than pressing and sintering. The powder was white before sintering and obtained a pink colour after sintering. Some additional dark orange sports were observed close to the edge.

Phase analysis by powder XRD

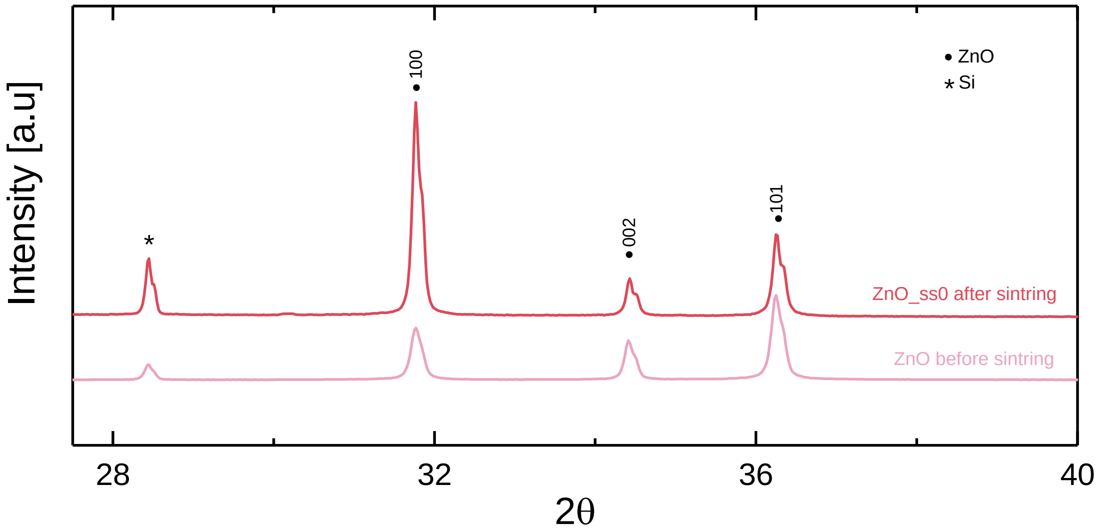

Figure 6.3: Powder XRD diffractogram obtained from powder of ZnO powder and from pellet after sintering. Three strong reflections for hexagonal wurtzite ZnO is present for 100, 002 and 101

Diffractogram obtained from powder XRD for phase analysis is presented in Figure 6.3. Three strong reflections for hexagonal wurtzite ZnO is present for 100, 002 and 101.

Investigation on microstructure by SEM

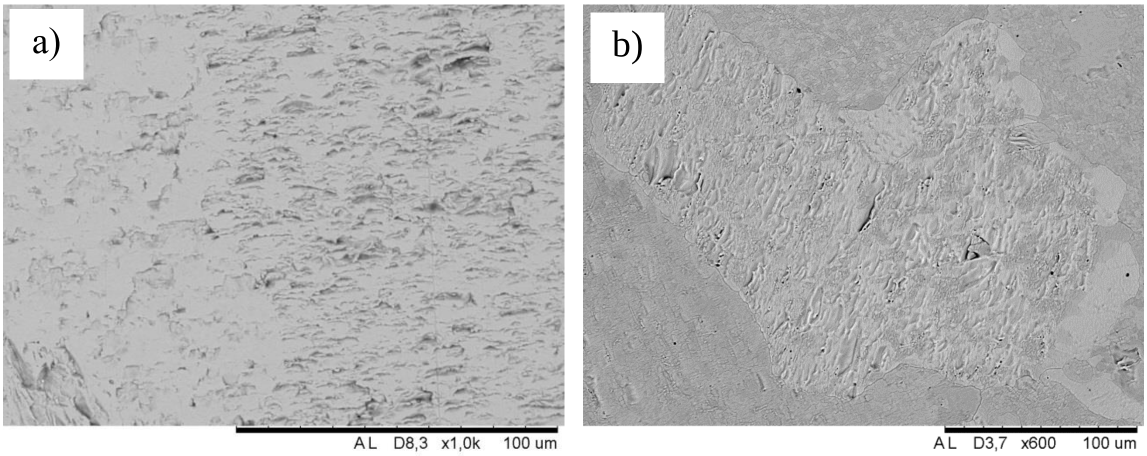

Figure 6.4: SEM images taken of the cross-section of the sample (a) and of the thermally etched sample (b).

Microstructure of the sample was investigated by SEM, presented in Figure 6.4. The polished cross-section is shown in a) and the thermally etched sample in b). The grain observed to the right is one of the smaller grains observed during investigation, due to larger grain getting harder to detect because the contrast gets poorer with decreasing magnification. The grain has in irregular form and some pores detected close to the grain boundary.

Appendix C

Crucible and as sintered samples

Image taken of samples after sintering and the crucible is shown in Figure 6.5. The characterization of the white layer by XRD is shown in Figure 6.6.

Figure 6.5: Image taken of the crucible and samples after sintering showing a white $ZnAl_2O_4$ layer on the samples with 5 mol% Al and the crucible, while the pure ZnO sample (to he right) doesn't have any additional powder.

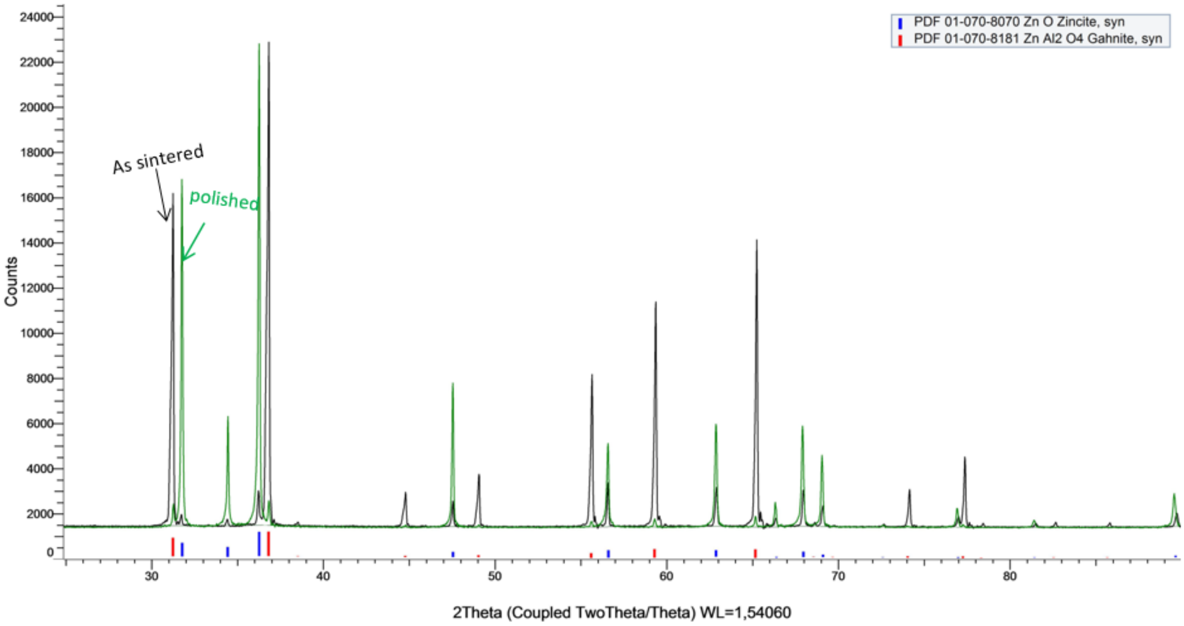

Figure 6.6: XRD taken of 5 mol% sample as sintered (black) and after polishing (green) shows that the white layer correspond to the $ZnAl_2O_4$ phase.

Appendix D

XRD of powder obtained after calcination for sol-gel

XRD for powder obtained after first calcination at 500°C, second calcination at 900°C and after sintering at 1500°C is shown in Figure 6.7 to illustrate the crystallization of ZnO after the second calcination.

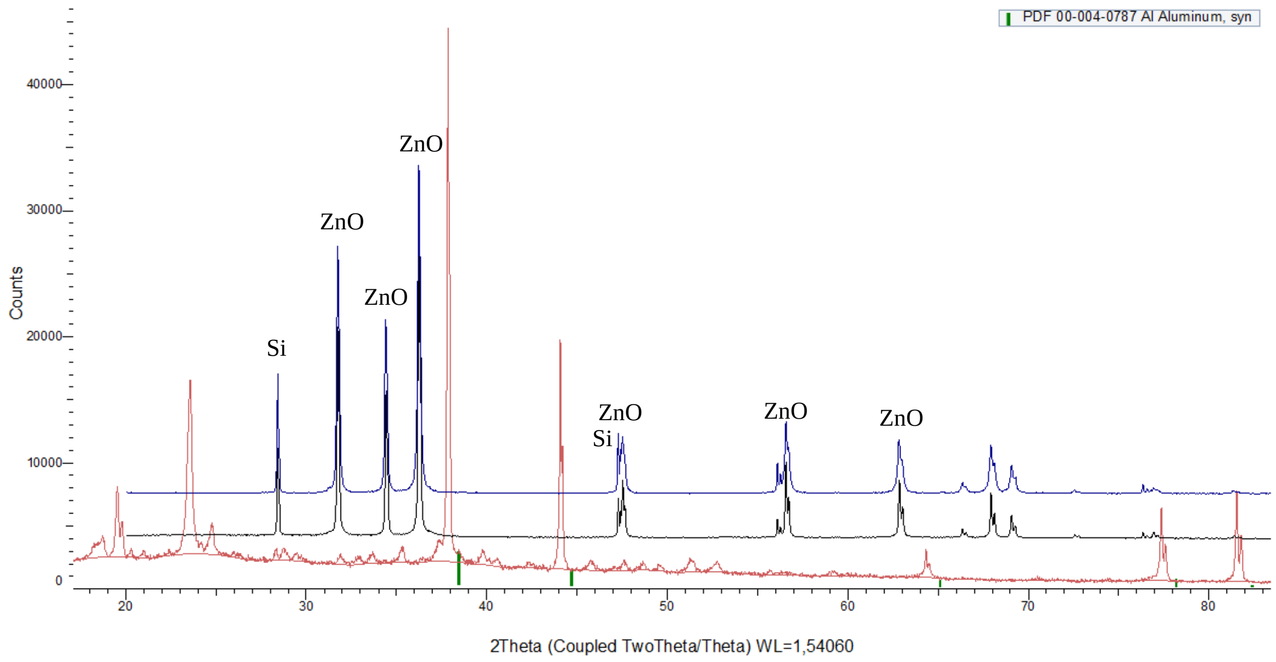

Figure 6.7: XRD for powder obtained after first calcination at 500°C (red), second calcination at 900°C (black) and after sintering at 1500°C (blue). Intense peaks close to the green lines corresponds to the alumina sample holder.

Appendix E

XRD of Al$_2$O$_3$

XRD taken of Al3O2 powder and ZnO with 5 mol% Al after ball milling is shown in Figure 6.8

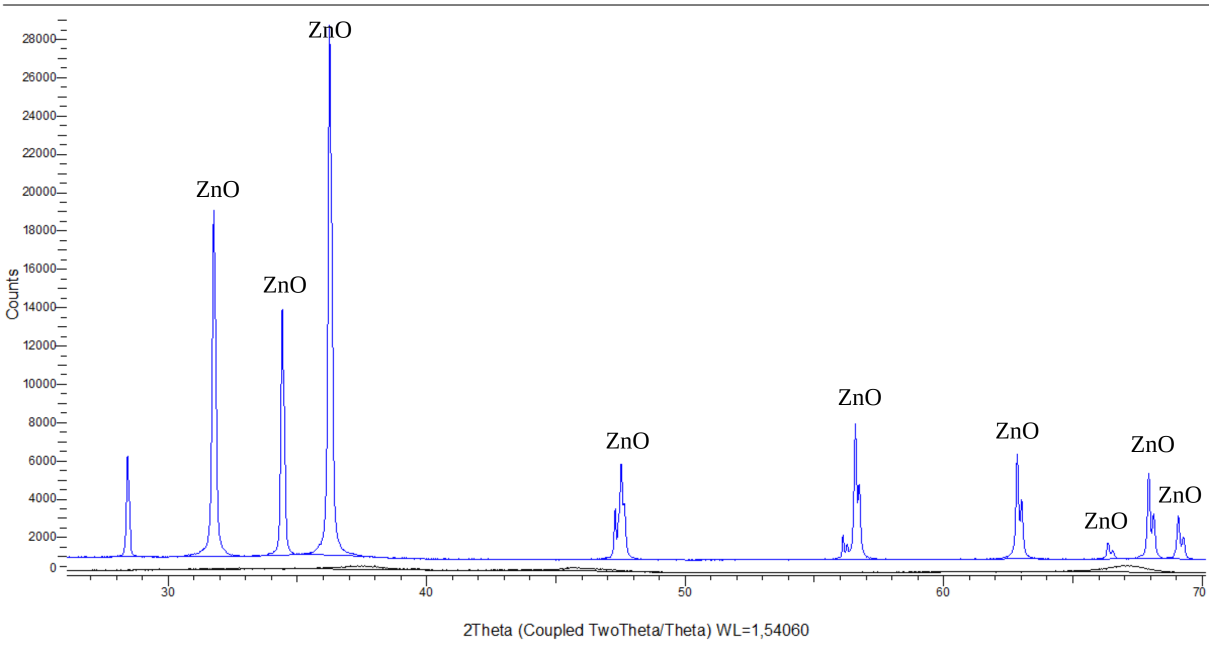

Figure 6.8: XRD taken of Al$_2$O$_3$ powder (black) and ZnO with 5 mol% Al content after ball milling. Very broad peaks are observed for Al$_2$O$_3$.

Appendix F

Remeasurements of samples prepared by solid state synthesis with planetary ball milling

Remeasurements of electrical conductivity and Seebeck coefficient is shown in Figure 6.9

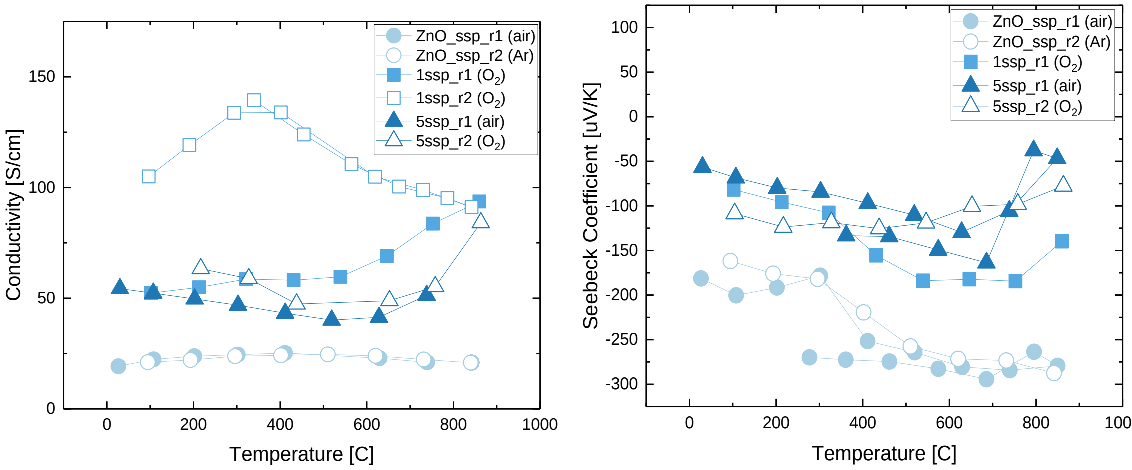

Figure 6.9: Remeasurements of electrical conductivity and Seebeck coefficient of sample prepared by solid state synthesis with planetary ball millling. No large changes was observed, beside change of electrical conductivity behavior for 1ssp. However, the same trend was followed while cooling.

Bibliography

1. Rowe, D.M., *Thermoelectrics Handbook.* 1 ed. Macro to Nano. 2005.

2. Snyder, G.J. and E.S. Toberer, *Complex thermoelectric materials.* Nature materials, 2008. **7**(2): p. 105.

3. Ohtaki, M., *Recent aspects of oxide thermoelectric materials for power generation from mid-to-high temperature heat source.* Journal of the Ceramic Society of Japan, 2011. **119**(1395): p. 770-775.

4. Terasaki, I., Y. Sasago, and K. Uchinokura, *Large thermoelectric power in* $NaCo_2O_4$ *single crystals.* Physical Review B, 1997. **56**(20): p. R12685.

5. Tritt, T.M. and M. Subramanian, *Thermoelectric materials, phenomena, and applications: a bird's eye view.* MRS bulletin, 2006. **31**(3): p. 188-198.

6. Chen, Z.-G., et al., *Nanostructured thermoelectric materials: Current research and future challenge.* Progress in Natural Science: Materials International, 2012. **22**(6): p. 535-549.

7. Ozgur, U., D. Hofstetter, and H. Morkoc, *ZnO devices and applications: a review of current status and future prospects.* Proceedings of the IEEE, 2010. **98**(7): p. 1255-1268.

8. Chou, Y.-H., et al., *Preparation and characterization of solid-state sintered aluminum-doped zinc oxide with different alumina contents.* Bulletin of Materials Science, 2011. **34**(3): p. 477-482.

9. Ohtaki, M., et al., *High‐temperature thermoelectric properties of* $(Zn_{1-x}Al_x)O$. Journal of applied physics, 1996. **79**(3): p. 1816-1818.

10. Tsubota, T., et al., *Thermoelectric properties of Al-doped ZnO as a promising oxide material for high-temperature thermoelectric conversion.* Journal of Materials Chemistry, 1997. **7**(1): p. 85-90.

11. Cai, K.F., et al., *Preparation and thermoelectric properties of Al-doped ZnO ceramics.* Materials Science and Engineering B-Solid State Materials for Advanced Technology, 2003. **104**(1-2): p. 45-48.

12. Jood, P., et al., *Al-doped zinc oxide nanocomposites with enhanced thermoelectric properties.* Nano letters, 2011. **11**(10): p. 4337-4342.

13. Nam, W.H., et al., *High-temperature charge transport and thermoelectric properties of a degenerately Al-doped ZnO nanocomposite.* Journal of Materials Chemistry, 2012. **22**(29): p. 14633-14638.

14. Han, L., *High Temperature Thermoelectric Properties of ZnO Based Materials*. 2014, Department of Energy Conversion and Storage, Technical University of Denmark.

15. Schubert, U., *Synthesis of inorganic materials*. 3rd compl. rev. and enl. ed, ed. N. Hüsing. 2012, Weinheim: Wiley.

16. Danks, A., S. Hall, and Z. Schnepp, *The evolution of 'sol–gel'chemistry as a technique for materials synthesis.* Materials Horizons, 2016. **3**(2): p. 91-112.

17. Gorrasi, G. and A. Sorrentino, *Mechanical milling as a technology to produce structural and functional bio-nanocomposites.* Green Chemistry, 2015. **17**(5): p. 2610-2625.

18. Norby, T., *Defects and transport in crystalline materials* 2016.

19. Tanaka, H., et al., *Strongly connected ex situ MgB2 polycrystalline bulks fabricated by solid-state self-sintering.* Superconductor Science and Technology, 2012. **25**(11): p. 115022.

20. Leng, Y., *Materials characterization : introduction to microscopic and spectroscopic methods*. 2nd ed. ed. 2013, Weinheim: Wiley-VCH.

21. Williams, D.B., *Transmission electron microscopy : a textbook for materials science*. 2nd ed. ed, ed. C.B. Carter. 2009, New York: Springer.

22. Wragg, D. *Powder X-ray Diffraction Theoretical Basis* [Lecture notes].

23. Waeselmann, N., *Structural transformations in complex perovskite-type relaxor and relaxor-based ferroelectrics at high pressures and temperatures.* 2012.

24. Tomlins, G.W., J.L. Routbort, and T.O. Mason, *Zinc self-diffusion, electrical properties, and defect structure of undoped, single crystal zinc oxide.* Journal of applied physics, 2000. **87**(1): p. 117-123.

25. Schmidt-Mende, L. and J.L. MacManus-Driscoll, *ZnO–nanostructures, defects, and devices.* Materials today, 2007. **10**(5): p. 40-48.

26. Tilley, R.J.D., *Understanding solids : the science of materials*. 2nd ed. ed. 2004, Chichester: Wiley.

27. Kittel, C., *Introduction to solid state physics*. 8th ed. ed, ed. P. McEuen. 2005, Hoboken, N.J: Wiley.

28. Tritt, T.M., *Thermal conductivity : theory, properties, and applications*. Physics of solids and liquids. 2004, New York: Kluwer Academic/Plenum Publishers.

29. Slack, G.A. and S. Galginaitis, *Thermal conductivity and phonon scattering by magnetic impurities in CdTe.* Physical Review, 1964. **133**(1A): p. A253.

30. Medlin, D. and G. Snyder, *Interfaces in bulk thermoelectric materials: a review for current opinion in colloid and interface science.* Current Opinion in Colloid & Interface Science, 2009. **14**(4): p. 226-235.

31. Sootsman, J.R., et al., *High thermoelectric figure of merit and improved mechanical properties in melt quenched PbTe–Ge and PbTe–Ge*$_{1-x}$*Si*$_x$ *eutectic and hypereutectic composites.* Journal of Applied Physics, 2009. **105**(8): p. 083718.

32. Lan, Y., et al., *Structure study of bulk nanograined thermoelectric bismuth antimony telluride.* Nano letters, 2009. **9**(4): p. 1419-1422.

33. Gelbstein, Y., et al., *High Thermoelectric Figure of Merit and Nanostructuring in Bulk p-type Ge*$_x$*(Sn*$_y$*Pb*$_{1-y}$*)*$_{1-x}$*Te Alloys Following a Spinodal Decomposition Reaction.* Chemistry of Materials, 2009. **22**(3): p. 1054-1058.

34. Kang, C., et al., *Comparison of thermal conductivity in nanodot nanocomposites and nanograined nanocomposites.* Applied Physics Letters, 2010. **96**(21): p. 213114.

35. Bux, S.K., et al., *Glass-like lattice thermal conductivity and high thermoelectric efficiency in Yb 9 Mn 4.2 Sb 9.* Journal of Materials Chemistry A, 2014. **2**(1): p. 215-220.

36. Zevalkink, A., et al., *Thermoelectric properties of Sr 3 GaSb 3–a chain-forming Zintl compound.* Energy & Environmental Science, 2012. **5**(10): p. 9121-9128.

37. Fleurial, J.-P., T. Caillat, and A. Borshchevsky. *Skutterudites: an update*. in *Thermoelectrics, 1997. Proceedings ICT'97. XVI International Conference on*. 1997. IEEE.

38. Schrade, M., et al., *Versatile apparatus for thermoelectric characterization of oxides at high temperatures.* Review of Scientific Instruments, 2014. **85**(10): p. 103906.

39. Norby, T., *EMF method determination of conductivity contributions from protons and other foreign ions in oxides.* Solid State Ionics, 1988. **28**: p. 1586-1591.

40. Vorobyeva, E.A., et al., *Heat Propagation in Anisotropic Heterogeneous Polymer-CNT Composites.* Journal of Composites Science, 2017. **1**(1): p. 6.

41. Suryanarayana, C., *Mechanical alloying and milling.* Progress in materials science, 2001. **46**(1-2): p. 1-184.

42. Han, L., et al., *The influence of α-and γ-Al2O3 phases on the thermoelectric properties of Al-doped ZnO.* Journal of Alloys and Compounds, 2013. **555**: p. 291-296.

43. Bérardan, D., C. Byl, and N. Dragoe, *Influence of the Preparation Conditions on the Thermoelectric Properties of Al-Doped ZnO.* Journal of the American Ceramic Society, 2010. **93**(8): p. 2352-2358.

44. Ma, N., et al., *Microstructure and thermoelectric properties of Zn*$_{1-x}$*Al*$_x$*O ceramics fabricated by spark plasma sintering.* Journal of Physics and Chemistry of Solids, 2010. **71**(9): p. 1344-1349.

45. de Lara Andrade, J., et al., *Effects of Al*$^{3+}$ *concentration on the optical, structural, photocatalytic and cytotoxic properties of Al-doped ZnO.* Journal of Alloys and Compounds, 2017. **729**: p. 978-987.

46. Zhang, Y., et al., *The Solubility and Temperature Dependence of Resistivity for Aluminum‐Doped Zinc Oxide Ceramic.* International Journal of Applied Ceramic Technology, 2012. **9**(2): p. 374-381.

47. Cheng, H., et al., *Characterization of Al-doped ZnO thermoelectric materials prepared by RF plasma powder processing and hot press sintering.* Ceramics International, 2009. **35**(8): p. 3067-3072.

48. Motloung, S.V., et al., *Effects of annealing time on the structure and optical properties of* $ZnAl_2O_4/ZnO$ *prepared via citrate sol-gel process.* Materials Today Communications, 2018. **14**: p. 294-301.

49. Wang, S.-F., et al., *A comparative study of* $ZnAl_2O_4$ *nanoparticles synthesized from different aluminum salts for use as fluorescence materials.* Scientific reports, 2015. **5**: p. 12849.

50. Chen, K.-J., et al., *The crystallization and physical properties of Al-doped ZnO nanoparticles.* Applied surface science, 2008. **254**(18): p. 5791-5795.

51. Kulkarni, A.J. and M. Zhou, *Size-dependent thermal conductivity of zinc oxide nanobelts.* Applied physics letters, 2006. **88**(14): p. 141921.

52. Jones, R., et al., *Organic Compounds of Uranium. V. Derivatives of Uranium (V) Alkoxides.* Journal of the American Chemical Society, 1956. **78**(23): p. 6027-6030.

53. Hansson, R., P.C. Hayes, and E. Jak, *Experimental study of phase equilibria in the Al-Fe-Zn-O system in air.* Metallurgical and Materials Transactions B, 2004. **35**(4): p. 633-642.